TOWARDS NEW EXPERIMENTALLY VALIDATED CRYSTAL PLASTICITY MODELS FOR POLYCRYSTALLINE METALS.

A Thesis
Presented to
The Academic Faculty

by

Nathan Bieberdorf

In Partial Fulfillment
of the Requirements for the Degree
Masters of Science in the
George W. Woodruff School of Mechanical Engineering

Georgia Institute of Technology
August 2018

TOWARDS NEW EXPERIMENTALLY VALIDATED CRYSTAL PLASTICITY MODELS FOR POLYCRYSTALLINE METALS.

Approved by:

Dr. Antonia Antoniou, Co-Advisor
School of Mechanical Engineering
Georgia Institute of Technology

Dr. Laurent Capolungo, Co-Advisor
School of Mechanical Engineering
Georgia Institute of Technology

Dr. Shuman Xia
School of Mechanical Engineering
Georgia Institute of Technology

Date Approved: May 14, 2018

In memory of Sanat Moningi;

a great friend, a great person.

ACKNOWLEDGEMENTS

TABLE OF CONTENTS

LIST OF TABLES

LIST OF FIGURES

image.

LIST OF SYMBOLS AND ABBREVIATIONS

S Surface

A Area

V Volume

x Coordinate in x-direction (horizontal)

y Coordinate in y-direction (vertical)

u Displacement in x-direction

v Displacement in y-direction

i Component in x-direction

j Component in y-direction

$\boldsymbol{\varepsilon}, \varepsilon_{ij}$ Strain tensor, component

$\boldsymbol{\varepsilon}^e, \varepsilon_{ij}^e$ Elastic strain tensor, component

$\boldsymbol{\varepsilon}^p, \varepsilon_{ij}^p$ Plastic strain tensor, component

$\boldsymbol{\sigma}, \sigma_{ij}$ Stress tensor, component

$\mathbf{x}$ Position vector

$\mathbf{r}, r$ Radial distance vector, magnitude

t Time

l Length

T Temperautre

k Boltzmann constant

C_{im} Two-point correlation function

I_{im} Image intensity

r_s Digital image correlation (DIC) subset window radius

$\mathbf{b}, b, b_i$	Burgers vector, magnitude, component
$\mathbf{n}, n_i$	Normal vector, component
$\mathbf{m}, m_{ij}$	Schmid tensor, component
ρ	Dislocation density
v	Velocity
$\dot{\gamma}$	Plastic slip rate
τ	Shear stress magnitude resolved on slip system.
α	Dislocation self-interaction hardening term
K	Forest dislocation source term
C_1, C_2, C_3	Forest dislocation contribution terms
n_0	Power-law exponent
λ	Lamé constant
μ	Shear modulus
v	Poisson's ratio
δ_{ij}	Kronecker delta
$\mathbf{C}, C_{ijkl}$	Fourth-order stiffness tensor, component
$\mathbf{\Gamma}^0$	Modified Green operator
$\mathbf{I}$	Identity tensor
$\mathbf{K}$	Fourth-order dilatational operator
λ_I	Image resolution
λ_G	Grain resolution
G_s	Gaussian speckle function
$\tilde{p}$	Speckle identifier
d_s	Characteristic length scale

Δ_{ij} DIC instrument resolution

c_1, c_2, c_3 Constants for DIC resolution equation

P Probability function

V Variance of probability density function

λ^s Mean spacing between microstructural obstacles

C_s Shear wave velocity

ρ_0 Mass density

h_{MX} Trapping coefficient for MX precipitate

ΔG Activation energy

χ Entropy factor

v_G Attempt frequency

R Proportion term

I_v Net vacancy flux

Ω Atomic volume

D_v Diffusion constant for vacancies

C_v Concentration of vacancies

$\mathbf{f}_c, f_c$ Peach-Kohler force, climb component

$\mathbf{t}$ Unit tangent vector

S_f Entropy for vacancy formation

E_f Energy for vacancy formation

g_0, g_1, g_2, g_3 Constants for vacancy formation and transport

k_1, k_2, k_3, k_c Dislocation density evolution terms

f_e Recovery parameter

λ_{sg} Sub-grain size

k_p Width of numerical integration bin

n_p Number of integration points

p, q Exponent factors for activation energy

m Exponent for hardening superposition

f Material porosity

h Geometry factor for void volume

ψ Angle of void edge with respect to grain boundary

$\bar{b}$ Mean spacing

a Void radius

ti Total number of time steps, or current time

$\tilde{n}$ Number density

$\bar{\sigma}$ Flow stress

$\mathcal{D}$ Diffusion term

α_n, β_n Hardening constants

n Hardening exponent

γ_s Free surface energy

δ_B Diffusion area thickness

L Effective length of diffusion

κ Void coalescence factor

ϕ Plastic potential

q_1, q_2 Constants for Gurson-Tvergaard-Needleman (GTN) model

d Damage term

SUMMARY

To enhance the current materials design paradigm, a vastly improved understanding of structure-property relationships across a wide range of material systems is required. Recent initiatives have highlighted the importance of using a synthesized approach of experiment and modeling to further elucidate these relationships. Numerical models should aim to robustly predict the effect of different microstructural features on material response, but certainly require validation against relevant experimental data, ideally on several different length scales.

With this in mind, experimental in-plane deformation maps as a tool for mesoscale calibration is presented. First, an investigation of the errors associated with experimental strain maps from Digital Image Correlation (DIC) and methods for optimizing experimental and numerical protocols to reduce uncertainty are presented. Second, a method to employ in-plane strain maps in calibrating a high-order numerical model is presented, highlighting the ability of the experimental dataset to further reduce the parameter space determined from experimental macroscopic load-displacement data. Lastly, a new, microstructurally-sensitive creep damage model is proposed and employed in a finite-element framework, and shows excellent agreement with experimental data, especially in the tertiary creep regime.

CHAPTER 1. INTRODUCTION

1.1 Materials Science by Design

Critical advancements in medicine, energy, transportation, and virtually all other fields of technology are enabled by the discovery and development of new materials with innovative and unique property combinations. However, the current materials design paradigm is one based mostly on a trial-and-error approach, where materials are iteratively generated and tested against their application requirements. This strategy is inefficient and expensive, which makes material innovation the limiting factor in the design of new technologies.

Ideally, materials could be designed for their applications from the start, in a process where different ingredients of materials science are aggregated to produce desired functionality. Projects like the Materials Genome Initiative (MGI) have recognized this potential for an improved materials design infrastructure. MGI proposes changing the current, disjointed linear materials development continuum in favor of a more iterative cycle where different stages of design are mixed, therefore acknowledging their codependence. The overall goal of MGI is to reduce by half, for a given material, the time from laboratory concept to wide-scale market adoption [1, 2].

Vital to the success of this goal are robust models that can predict material behavior based on a wide range of inputs. Multiscale modeling efforts, such as Integrated Computational Materials Engineering (ICME), aim to explicitly describe the physical processes occurring on different length scales and how they aggregate to a bulk response

[3, 4]. Intuitively, only physically-justified descriptions of material response will provide accurate predictions of behavior across many applications, when compared to empirical relations alone.

In order to validate such models, comparison with experimental data is of course necessary, and should be accomplished on several different length scales. Indeed, it has been shown that bulk response characterization is not sufficient in identifying the unique set of parameters for a numerical model. Therefore, a co-design approach to experimentation is encouraged, where domains of theory and experiment are in direct communication so that they will iteratively produce datasets which are considered valuable to both sides [5].

1.2   Thesis Plan

With these objectives in mind, this thesis demonstrates a synthesized approach to experiment design. First, in Chapter 2, the experimental approach is described, where digital image correlation (DIC) is studied for its accuracy in measuring the heterogeneous strain fields from a polycrystalline material system. Several sources of uncertainty are thoroughly investigated, and a tool for determining the instrument resolution of DIC is presented.

In Chapter 3, the role of DIC-measured strain in parameterizing a high-order numerical model is studied. The model is implemented in a finite-element framework, allowing for a full-field material response prediction. Since it is shown that comparison with experiment on the bulk-scale alone can "validate" several varying parameter

combinations, it is postulated that comparison on the mesoscale, using DIC-measured strain fields, can further reduce the parameter space.

In Chapter 4, a new microstructurally-sensitive damage model for the creep behavior of polycrystalline materials is presented. The model is founded on physical descriptions of local porosity evolution and is implemented in the same finite-element framework as Chapter 3. Numerical predictions of material response show excellent agreement with experimental data, especially in the tertiary creep regime.

CHAPTER 2.   TOWARDS QUANTITATIVE CRYSTAL PLASTICITY MODEL VALIDATION USING EXPERIMENTAL IN-PLANE DEFORMATION MAPS

2.1   Abstract

In this chapter, a crystal plasticity based constitutive model implemented in a high-resolution full-field Fast Fourier Transform (FFT) mechanical solver is used to perform a numerical experiment in an aluminum polycrystal subjected to uniaxial tension up to one percent strain. These FFT simulations provide for the 'true/reference' displacement and strain fields everywhere in the system. In parallel, images of experimentally generated DIC patterns are collected. The digitized patterns are then numerically displaced as dictated from the local reference displacements fields obtained from the polycrystal plasticity simulations. Comparing deformed and original patterns, DIC strain maps are generated with NCorr DIC software. Those DIC maps are then directly compared with the references strain maps obtained from the FFT simulations. Using this approach, it is shown that inexpensive DIC experiments can result in strain measurements of high enough quality to be *quantitatively* compared to models.

2.2   Background

Typically, constitutive models are calibrated against stress-relaxation, uniaxial, or multi-axial tests where the texture evolution is also monitored [6]. Further, it has been proposed to use either the dislocation content extracted from diffraction peak profile analysis [7] or the breadth of diffraction lines as metrics for calibrating constitutive

4

models. However, the aforementioned characterization methods produce metrics lacking spatial resolution. Digital Image Correlation (DIC) is a scale agnostic, in-situ experimental mapping technique that tracks displacement of patterned surface features during loading. DIC may be used to obtain full-field surface strain maps from the measured displacement fields, but it should be noted that highly inhomogeneous deformation fields of polycrystalline metals pose significant challenges for DIC. Several approaches have been proposed to address these issues. This includes use of high-resolution optics and patterns [8-10], and development of DIC algorithms achieving sub-pixel resolution. Following this idea, researchers were able to obtain integrated crystallographic and deformation data by coupling DIC with Electron Backscattering Detection (EBSD) [11-13].

Clearly, the prospect of automating model validation and rejection by using objective error functions is greatly appealing, and some attempts have been proposed in the literature [14], but a crucial step still remains in quantifying the limits in accuracy offered by DIC. A typical DIC experiment has several sources of error including, those associated with image acquisition, pattern quality and DIC algorithm limitations. This chapter aims to quantify the error from pattern quality and DIC parameter selection, and the context of these two factors is briefly discussed here.

First, in order to track surface feature displacement with high fidelity, a sample must have a low correlation between groups of pixels (i.e. be as randomized as possible), and as such, random "patterns" are applied often to a sample. The quality (randomness) of an applied pattern is therefore important. If separate groups of pixels within a pattern are quantitatively similar to one another, then a given subset can be "identified" at the

5

wrong coordinate location in a loaded image. Clearly, this will cause erroneous displacement and strain measurements.

For similar reasons, poor subset window size selection by the user can produce error in strain measurements. Since displacements are averaged within local subsets, it is intuitive that minimizing the subset radius will produce higher resolution strain mapping, especially for regions were deformation is highly localized. However, smaller subsets are more likely to be quantitatively similar in features, and therefore can produce errors of the same type described just above. Therefore selection of subset size is a balance between resolution and "noise" from erroneous subset identification.

2.3   Experimental Protocol

2.3.1   Pattern Generation and Classification

Pattern quality plays a crucial role in obtaining reliable measurements of strain and displacement from DIC. In this work, considerations are deliberately limited to patterns that can be realistically generated using an airbrush and applied on a metallic surface. Thirty-two speckle patterns were generated on an aluminum alloy surface using an Iwata CM-B 0.18 mm airbrush. The airbrush deposits paint particles on the surface as spherical globules in the ~5-30 µm range, with size and concentration depending on the paint viscosity, air pressure, distance between airbrush and sample, and spray aperture. A wide array of patterns was generated by varying these application techniques. In order to enhance the dynamic grey scale range, paints of different colors were used. Prior to pattern application, the sample was painted with a base white coat to conceal features inherent to the sample surface. The samples were imaged using an 8-bit Edmund Optics

camera with an image size of 1920 x 2560 pixels corresponding to a field of view of 2.1 x 2.7 mm. Lighting was maintained to minimize glare and shadow effects, and translated image pairs of each pattern were acquired during the process. For this work, four representative patterns are selected for focus, based a visual inspection of the dataset.

Patterns were characterized using several complementary techniques. First, a two-point correlation function is computed. It is defined as the following:

$$C_{im}(r) = \langle I_{im}(\mathbf{x}) I_{im}(\mathbf{x} + \mathbf{r}) \rangle \tag{1}$$

where I denotes the image intensity at material position $\mathbf{x}$, and $\langle ... \rangle$ denotes averaging over all positions $\mathbf{x}$. The patterns thus generated were found to be isotropic and therefore the correlation function only depends on the distance $r = |\mathbf{r}|$. The two-point correlation function can be used to estimate typical feature sizing, and overall image density [15, 16]. In a more qualitative sense, the correlation function reveals the probability that two points of an image, separated by distance r, will both be of the same feature type. The two-point correlation analysis was performed for patterns whose images were thresholded with the Otsu method using Image J [17].

Additionally, a cluster analysis of the binary patterns was used to obtain the diameter, centroid coordinates and population density of the speckles. The cluster analysis relied on a Hough Transformation method for locating imperfect instances on a particular shape in an image [18, 19]. With this method, circles of varying radii could be fit to speckles for each pattern. Additionally, fitted circles whose areal density was less

than 80% black were considered false positives and removed from analysis. Finally, normalized histograms of the patterns were examined.

2.3.2 In-plane Displacement and Strain from Digital Image Correlation

This work uses the open source 2D, subset-based DIC code, NCorr [20]. Subset-based DIC algorithms split a patterned image into smaller regions (subsets) and track where subsets move in subsequent images obtained during loading. For the case of NCorr, subsets are circular in shape, and are defined on the reference image at integer locations. Both the subset radius, r_s, as well as the subset spacing can be varied. The deformation in each subset is assumed to be a linear, first order transformation so that:

$$\begin{pmatrix} \tilde{x}_{ref_i} \\ \tilde{y}_{ref_j} \end{pmatrix} = \begin{pmatrix} x_{ref_i} \\ y_{ref_j} \end{pmatrix} + \begin{pmatrix} u_{rr} \\ v_{rr} \end{pmatrix} + \begin{pmatrix} \frac{\partial u}{\partial x_{rr}} & \frac{\partial u}{\partial y_{rr}} \\ \frac{\partial v}{\partial x_{rr}} & \frac{\partial v}{\partial y_{rr}} \end{pmatrix} \begin{pmatrix} x_{ref_i} - x_{ref_c} \\ y_{ref_j} - y_{ref_c} \end{pmatrix} \quad (i,j) \in S \qquad (2)$$

where $\tilde{x}_{ref_i}$ and $\tilde{y}_{ref_j}$ are the x and y coordinates of a deformed reference subset point. The "rr" subscript in Equation 2 is to delineate a transformation between two different coordinate systems in the reference image and subscript "c" denotes the center of the subset [20]. The location of the subset in the deformed configuration is found from the extrema of a correlation function defined from the convolution of gray scale values of the reference and subsequent images. For NCorr, a nonlinear optimizer, e.g. Inverse Compositional Gauss-Newton (ICGN), is further used to obtain subset displacements with sub-pixel resolution through interpolation with biquintic B-splines of the gray scale images. The above analysis procedure provides in-plane displacements u and v with sub-pixel resolution for each subset center, "c". NCorr obtains in-plane strains from the

8

gradients of a least-square plane fit of a group of points in the displacement field. From the above discussion, each DIC analysis can give displacements for a given subset window size and subset window overlap. The strain field can be obtained by performing a least-square plane fit over a group of points of size w_e from the displacement field. In this work an examination of the difference in strain fields as a function of subset window radius, r_s, are conducted for a polycrystalline metal with a highly heterogeneous deformation field.

2.3.3 Rigid-Body Translation

Quality assessment of patterns and image acquisition is often done by DIC analysis of the pattern after a simple translation without imposing a load. Rigid body translation (RBT) of an object does not cause deformation and therefore under such a transformation the strain fields should be zero. Any measured strain field values set an effective low limit of the resolution of DIC. Effectively, this is the minimal error in the analysis and is irreducible. Images of the generated patterns were obtained experimentally before and after the sample was translated by approximately 10 µm without any load applied. In addition, an image from each pattern was digitally translated by similar magnitude using interpolation functions, whose uncertainty is quantified in Section 2.5.3. Both experimentally and numerically translated image pairs were analyzed using NCorr [20, 21] and the resulting displacements (u, v) were obtained for different subset window radii of r_s = 15, 25, and 50 pixels (~16.1, 26.8, and 53.5 µm) and an overlap of 1 pixel (~1.07 µm). The strains were calculated from the displacement fields using a strain window of 5 pixels (~5.4 µm). In the case of RBT, the average of absolute

measured strain, $\langle|\varepsilon_{ij}(x)|\rangle_{RBT}$, for each component ij and across every analysis site, x, is studied in subsequent analysis for each pattern and subset size.

2.4 Numerical Protocol

2.4.1 Crystal Plasticity Model

The constitutive model and calibration parameters used were originally proposed by Richeton et al. in [22]. The main elements of the model are therefore summarized in what follows. The plastic deformation and strain hardening induced by the slip of dislocations is accounted for by a conventional crystal plasticity framework rendering the evolution of mobile and sessile dislocation densities on slip systems as well as latent hardening [22]. The plastic slip rate tensor, $\dot{\boldsymbol{\varepsilon}}^p$, is:

$$\dot{\varepsilon}_{ij}^{p} = 1/2 \sum_{s} \rho^s b v^s \left(n_i^s b_j^s + n_j^s b_i^s \right) = \sum_{s} \dot{\gamma}^s m_{ij}^s, \tag{3}$$

where $\dot{\gamma}^s = \rho^s b v^s$ is the plastic slip rate on slip plane s of slip direction $\mathbf{b}^s$ and normal $\mathbf{n}^s$. The mobile dislocation density ρ^s in system s moves at an average velocity v^s. The magnitude of the Burgers vector of all 12 fcc slip systems is b, and $m_{ij}^s = 1/2(n_i^s b_j^s + n_j^s b_i^s)$ is the symmetrized orientation Schmid tensor. By denoting the Cauchy stress tensor $\boldsymbol{\sigma}$, plastic slip on system s is activated by the resolved shear stress $\tau^s = \boldsymbol{\sigma} : \mathbf{m}^s$ through the velocity power law

$$v^s = v_0 \left(\frac{|\tau^s|}{\tau_h^s + \tau_p} \right)^{n_0} \text{sign}(\tau^s). \tag{4}$$

10

In the above, v_0 and n_0 are respectively reference velocity and power law exponent. The term τ_h^s represents forest hardening on slip systems due to forest dislocation densities. Latent hardening is assumed in the following form [23]:

$$\tau_h^s = \mu b \sqrt{\sum_{s'} \alpha^{ss'} \rho_f^{s'}}, \tag{5}$$

where the latent hardening coefficient $\alpha^{ss'}$ provides the contribution of the forest density ρ_f^s on system s to hardening of system s'. A mean value $\alpha^{ss'}$ is taken for all these coefficients, except for collinear interactions, i.e. interactions involving the same Burgers vector, where the value α^{ss} is used. Such reaction is known to lead strong latent hardening effects. Starting from the initial values ρ_{m0} and ρ_{f0}, the evolution of slip system mobile and forest dislocation densities with plastic straining is given by the following rate laws:

$$\frac{\dot{\rho}_m^s}{\rho_{m0}} = \left(K_m - K_f + \frac{C_1}{\sqrt{\rho_{m0}}} \sum_s \sqrt{\rho_f^s} - \frac{C_2}{\rho_{m0}} \sum_s \sqrt{\rho_m^s \rho_f^s} \right) |\dot{\gamma}^s|, \tag{6}$$

$$\frac{\dot{\rho}_f^s}{\rho_{f0}} = \left(K_f + \frac{C_2}{\rho_{m0}} \sum_s \sqrt{\rho_m^s \rho_f^s} - \frac{C_3}{\rho_{m0}} \rho_f^s \right) |\dot{\gamma}^s| \tag{7}$$

In the above, K_m and K_f reflect mobile and forest dislocation source terms, C_1, C_2, and C_3 account respectively for the contribution of forest dislocation to mobile dislocation sources, the arrest of mobile dislocations due to interactions with forest dislocations, and

11

dynamic recovery. All material parameters, listed in Table 1, were obtained from [22] by fitting against experimental results.

Table 1. Constants used in FFT numerical model

Parameter		Al alloy [22]
n_0	Power-law exponent	20
v_0	Reference velocity	5×10^{-10} m/s
ρ_{m0}	Initial mobile dislocation density	$22 \times 10^9 \text{m}^{-2}$
ρ_{f0}	Initial forest dislocation density	$22 \times 10^9 \text{m}^{-2}$
$\alpha^{ss'}$	Non-collinear dislocation hardening term	0.12
α^{ss}	Collinear dislocation hardening term	1.265
b	Burgers vector	2.862×10^{-10}m
K_m	Mobile dislocation source term	2.8×10^4
K_f	Forest dislocation source term	1.4×10^4
C_1	Forest-mobile dislocation contribution term	2.2×10^3
C_2	Arrest of mobile dislocations term	80
C_3	Dynamic recovery term	500
λ	Lamé constant	62 GPa
μ	Shear modulus	23 GPa

In order to obtain numerically the full field solution for the response of the medium, a Fast Fourier Transform approach is used. In a small strain framework, there is consideration of the elastic-plastic deformation of a body B subjected to external displacements **u** and tractions **T** on its external boundaries ∂B_u and ∂B_t. In the absence of body forces and inertia effects, the balance of the Cauchy stress tensor is:

$$\text{div } \boldsymbol{\sigma} = 0 \qquad (8)$$

Homogeneous linear isotropic elasticity is reasonably assumed in the case of aluminum:

$$\sigma_{ij} = \lambda \varepsilon_{kk}^e \delta_{ij} + 2\mu \varepsilon_{ij}^e. \qquad (9)$$

In the above, λ and μ are the Lamé constants. The tensor $\boldsymbol{\varepsilon}^e = \boldsymbol{\varepsilon} - \boldsymbol{\varepsilon}^p$ is the elastic strain tensor, $\boldsymbol{\varepsilon}$ and $\boldsymbol{\varepsilon}^p$ are the total and plastic strain tensors. Using Equation 8 together with the strain decomposition $\boldsymbol{\varepsilon} = \boldsymbol{\varepsilon}^e + \boldsymbol{\varepsilon}^p$, one can obtain:

$$\boldsymbol{\varepsilon} + \boldsymbol{\Gamma}^0 * (\delta\mathbf{C}:\boldsymbol{\varepsilon}) = \boldsymbol{\Gamma}^0 * (\mathbf{C}:\boldsymbol{\varepsilon}^p) + \mathbf{E} \tag{10}$$

where $\mathbf{E}$ is the applied mean strain and $\boldsymbol{\Gamma}_0$ is the modified Green operator. Here, $\mathbf{C} = 3\lambda\mathbf{K} + 2\mu\mathbf{I}$ is the 4th order stiffness tensor, and $\delta\mathbf{C} = \mathbf{C} - \mathbf{C}_0$, with $\mathbf{C}_0$ a fictitious stiffness tensor of a numerical reference medium. $\mathbf{I}$ is the fourth order identity tensor while $\mathbf{K}$ is the fourth order tensor extracting the dilatational component of any second order tensor. Validation of the model is shown in Figure 1, where a comparison between predictions of the mechanical response of single crystals subjected to monotonic and uniaxial loading along the [001], [112] and [123] directions are compared to experimental data [24].
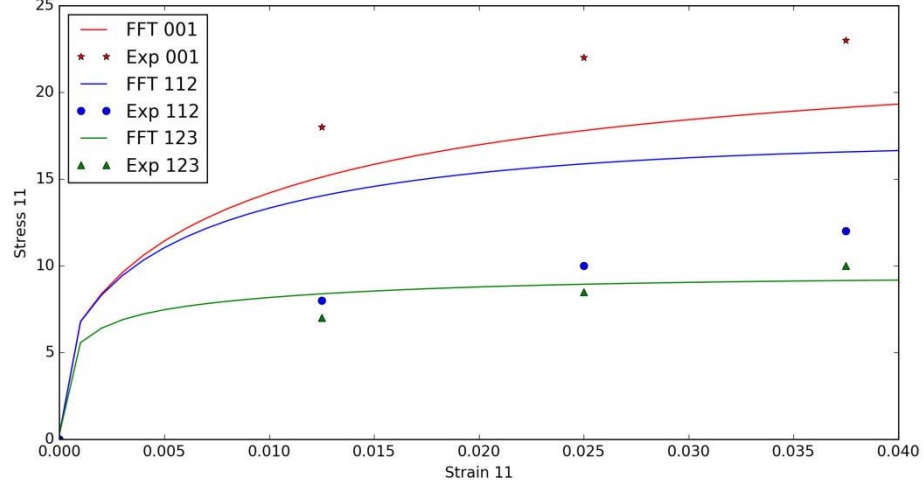
Figure 1. Model calibration parameters using single crystal testing under uniaxial loading along [001], [112] and [123] directions. Solid lines show the numerical prediction as compared to the experimental data.

2.4.2 Virtual Pattern Deformation

To provide a reference data set against which the accuracy of DIC approach can be quantified, the model is exercised to simulate plastic flow in a polycrystalline sample. To this end, a discretized grid of 1024x1024 voxels is employed, representing a total domain size of approximately 2.1mm x 2.1mm (to match the field-of-view of the camera used to image samples). A two-dimensional polycrystal, made of 100 grains, is generated by a standard Poisson-Voronoi procedure, with random grain orientation. This virtual sample is then subjected to a macroscopic mean strain with value $\varepsilon_{11} = 0.01$, $\varepsilon_{22} = \varepsilon_{33} = -\nu\varepsilon_{11}$, and using a strain rate of 1×10^{-4} s^{-1}. The loading is discretized into fixed time steps of 0.02 seconds, and the time integration of the crystal plasticity law made using a standard theta-method with $\theta = 0.5$.

An image from each speckle pattern was digitally strained using displacement fields from the two-dimensional (2D) polycrystalline aluminum alloy simulation. The

simulation field was mapped onto the image using high-order interpolation with all the associated interpolation errors carefully quantified (see Section 2.5.3). In addition, a reasonable size of 200 μm for Al grains, corresponding to an ASTM grain size of 2, was chosen for the simulation.

In the case of polycrystalline deformation simulation, the *local* of absolute difference, $\varepsilon_{ij}^{diff}(x)$, between the in-plane strains measured from DIC and the simulation at each analysis site, x, is studied and defined as:

$$\varepsilon_{ij}^{diff}(x) = \left| \varepsilon_{ij}^{sim}(x) - \varepsilon_{ij}^{DIC}(x) \right|. \qquad (11)$$

2.5   Results and Discussion

2.5.1   *Pattern Classification*

Figure 2 shows the grayscale images of four patterns selected for further analysis based on a visual examination. The four chosen patterns represent the greatest variation of features such as speckle areal density, speckle size and speckle spacing. P1 was created using four different colors (black, red, blue, and yellow), with a narrow spray aperture, at a distance far from the sample (7 inches). P2 was produced using black and yellow paint, with a wide aperture, applied very close to the sample (4 inches). P3 was produced using all four colors, with a wide aperture, applied very close to the sample. P4 was created using all four colors, with a wide aperture, at a distance far from the sample. P1 and P4 images can be used to examine the effect of spray aperture width on the pattern, P2 and P3 can be used to understand effect of using multiple colors, and P3 and P4 can be used to understand the effect of application distance.
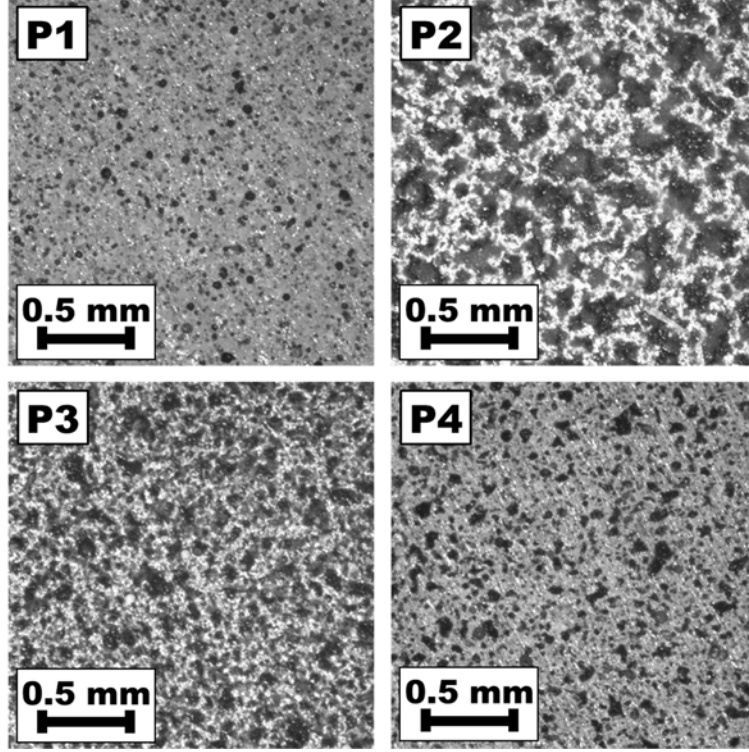
Figure 2. Four patterns (P1, P2, P3, and P4) created using airbrush painting techniques that vary in number of colors applied, spray aperture width, and distance between airbrush and sample.

Characterization by means of two-point correlation is presented in Figure 3(a). As the distance, r, increases, the correlation coefficient of each pattern decays rapidly until it reaches a plateau, which eventually approaches the relative area fraction of speckles in each image. The dashed horizontal lines, are the relative areal density. The function decreases most quickly for P1, indicating that the correlation between two points in the image rapidly decreases as distance between points, r, increases. The decrease for P4 and P3 is more gradual, while P2 maintains a high correlation for a larger magnitude of r. The characteristic length scale of each pattern is defined as the midpoint of the correlation coefficient of the plateau and the peak correlation coefficient value of 1. For each pattern, the midpoint is marked on Figure 3(a) by an asterisk. Using this technique, the smallest

16

characteristic scale is 17.3 μm for P1; followed by 21.0 μm for P4, 22.1 μm for P3 and 26.3 μm for P2.
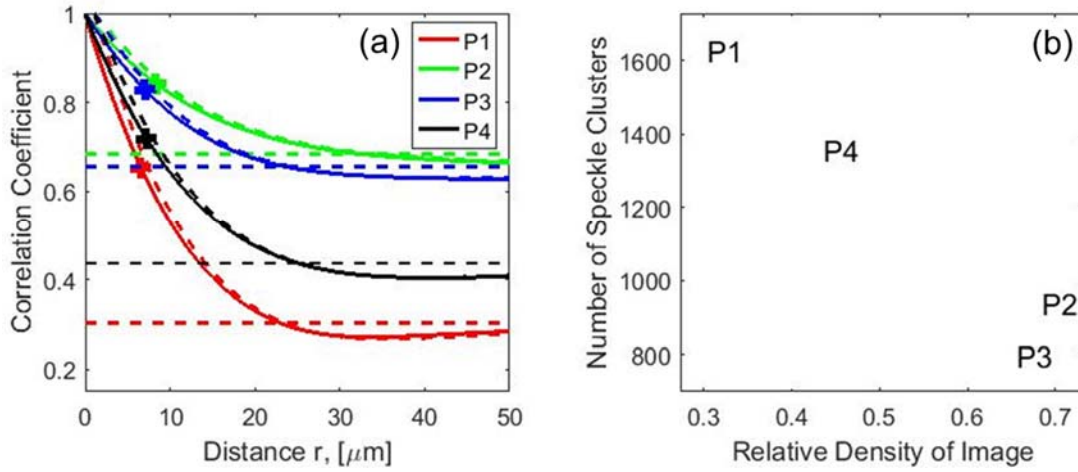
Figure 3. (a) Two-point correlation of the patterns P1-P4 as a function of characteristic scale (solid lines). (b) Calculated pattern area fraction and number of speckle clusters.

From the cluster analysis, Figure 3(b) shows the total speckle count as a function of the relative density of each pattern. P1 has a very high speckle count with low area fraction of dark speckles, while P2 and P3 have much lower speckle counts with high area fractions. P4 has a relatively medium speckle count and area fraction when compared to the other patterns.

Figure 4 shows histograms of the speckle size diameter and nearest speckle spacing for each pattern using cluster analysis of each thresholded image. The most frequently occurring speckle diameter for each pattern is found to be in close agreement with the size and ranking from the two point correlation calculation. Intricacies of the speckles are revealed from the cluster analysis histograms. For example, Figure 4(a) shows that P1 and P4 mainly consist of fine speckles with size 18.4 μm, with P4 also

17

having a 2% fraction of larger, ~55 µm, speckles. In contrast, P2 and P3 contain bimodal

speckle sizes with equal frequency of sizes 18.4 µm and 55 µm respectively. Figure 4(b)

shows the nearest speckle spacing histogram for each image. For P1 and P4, the speckles

are at a fairly consistent distance of 30-33 µm as ascertained from the most frequently

occurring distance and by the narrow distribution (within 50 µm). In contrast, P2 and P3

have a wider speckle distance distribution, within 80 µm.
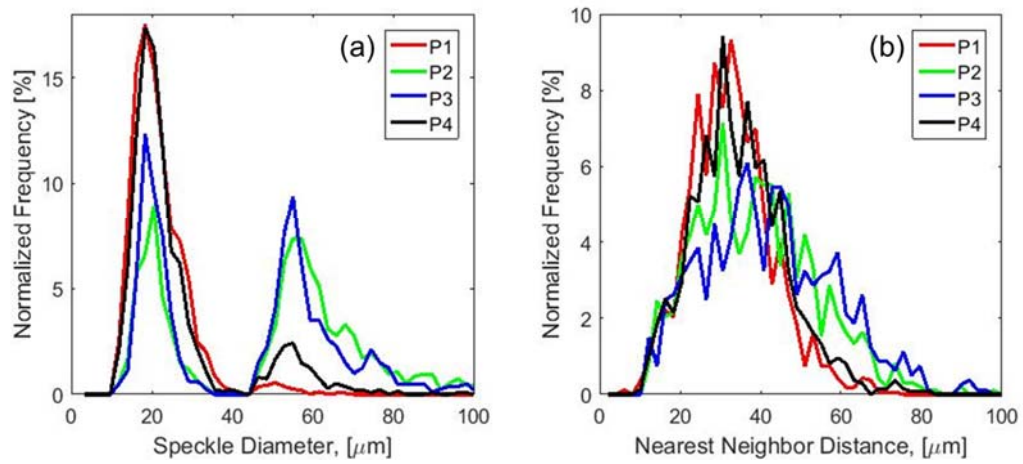
Figure 4. (a) Speckle diameter histogram from cluster analysis. (b) Center-to-center speckle spacing from cluster analysis.

Figure 5 presents the histograms of grayscale intensity for each pattern, which

span the range from 0 to 255, where 0 corresponds to black and 255 to white. It can be

seen that P1 and P2 have an average grayscale value of 138, with P1 having a narrower

distribution than P2. Patterns P3 and P4 have a grayscale average value of 130 with a

distribution closer to P2.
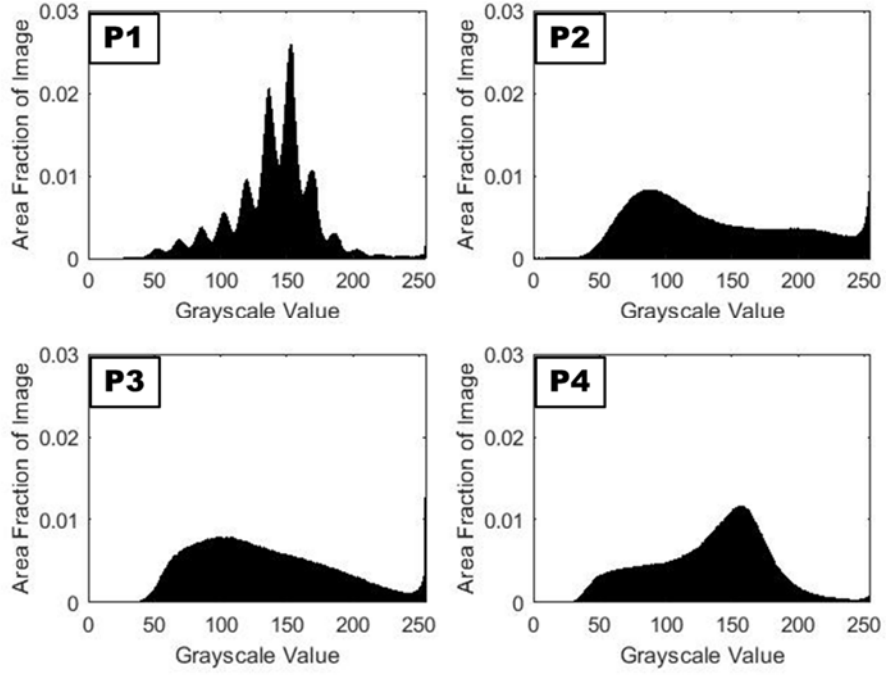
Figure 5. Normalized histograms of grayscale intensity for four patterns (P1, P2, P3, and P4).

2.5.2   Pattern Performance in Digital Image Correlation

2.5.2.1   Rigid Body Translation

Results from RBT analysis are presented in Figure 6, where the mean of absolute in-plane DIC calculated strains, $\langle |\varepsilon_{ij}(x)| \rangle_{RBT}$, for each ij strain component is plotted from the numerical RBT analysis (top row) and the experimental RBT analysis (bottom row) of the four patterns.
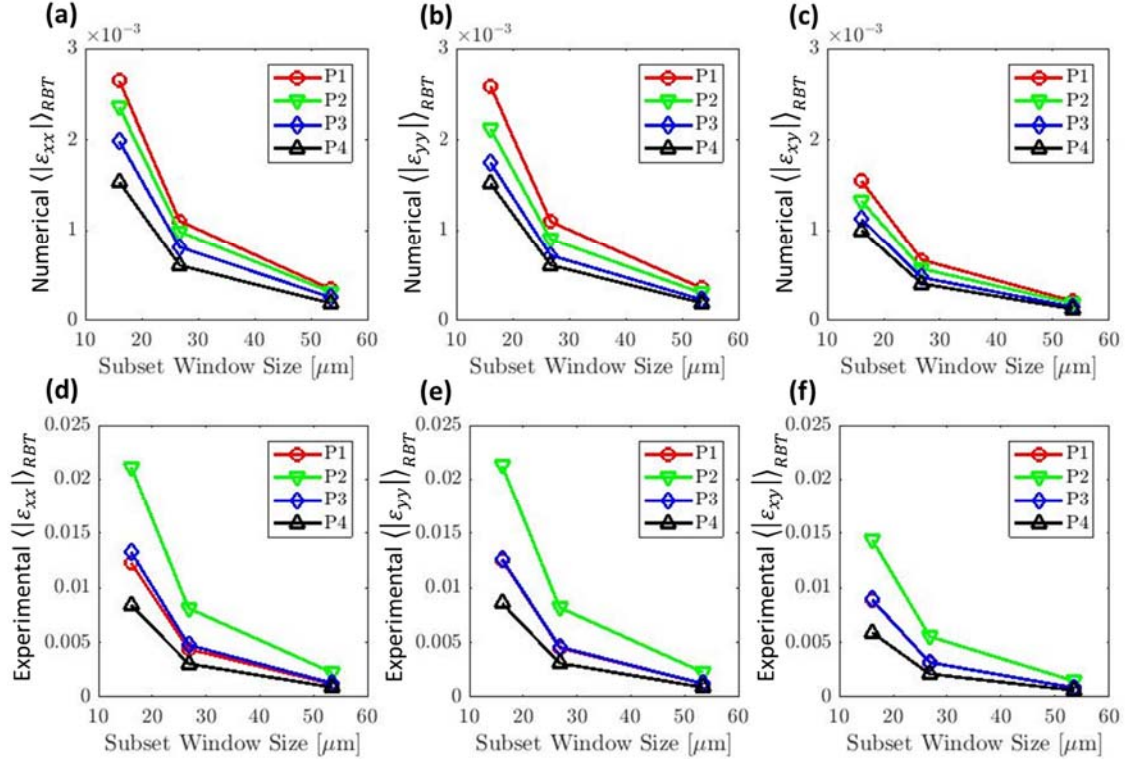
Figure 6. Mean absolute difference in strain components, ε_xx (first column), ε_yy (second column), ε_xy (third column), as a function of subset window radius measured using numerical RBT (top row) and experimental RBT (bottom row), for each pattern.

It can be seen that as the subset window size increases, the deviations in DIC measurements decrease by nearly one order of magnitude for all numerically translated patterned samples. Numerical RBT results are similar between axial, ε_{xx}, and transverse, ε_{yy}, strains, where P1 has the largest deviation from zero, which decreases from 2.6×10^{-3} to 3.5×10^{-4} when increasing the subset window from ~15 to 50 μm. Numerical data from P4 always have the smallest deviation from zero, decreasing from 1.5×10^{-3} to 1.9×10^{-4} for axial and transverse strains, when increasing from the smallest subset window size to the largest. DIC deviation from zero for shear strain, ε_{xy}, is slightly lower: P1 decreases from 1.6×10^{-3} to 2.2×10^{-4} and P4 from 1.0×10^{-3} to $1.2 \times$

10^{-4}. The ranking in terms of accuracy for patterns based on numerical RBT is consistently *P4, P3, P2, P1*. When $r_s\sim 15$ μm, the RBT estimated uncertainty for the worst pattern (P1) is 70% greater than the best (P4). When $r_s\sim 15$ μm, difference between the best (P4) and worst pattern (P1) is 50%.

The pattern ranking using the RBT analysis is not the same between the numerical and experimental dataset. From the experimental RBT dataset, the largest deviation is seen in P2 and it reduces from 2.2×10^{-2} to 2×10^{-3} as subset window radius increases from ~15 μm to ~50 μm for both $\varepsilon_{xx}, \varepsilon_{yy}$. For P1, the RBT deviation reduces from 1.2×10^{-2} to 1×10^{-3} as subset window radius increases from ~15 μm to ~50 μm for both $\varepsilon_{xx}, \varepsilon_{yy}$. The reduction in deviation for P3 is similar to P2, and for P4 it is 8×10^{-3} to 5×10^{-5} as subset window radius increases from ~15 μm to ~50 μm. The ranking therefore based on experimental RBT is *P4, P1, P3, P2.*

From both experimental and numerical RBT analysis, it can be seen that, for the case of uniform deformation, there is a substantial reduction in the error when a larger subset is used. This is intuitive since a larger region on which to perform analysis allows one to remove small perturbations stemming from low correlation sites.

Additionally, it can be seen DIC deviations from experimental RBT data are consistently greater than numerical by a factor of approximately 5. Such increased deviation is likely rooted in the image acquisition system, where uneven lighting gradient (glare and shadow), lens distortion, or inherent camera quality can introduce uncertainty into the system. While important to note for application purposes, the discussion of these variables is not within the scope of this study.

Regardless, both numerical and experimental RBT analyses give a measure of the irreducible error in system and show that even with all additional concerns from experimental imaging sources, the differences in strain are of the order of 10^{-3} when using a high quality pattern. Demonstrated in the proceeding text, this DIC technique is used to measure strains on the order of 10^{-2}, to map heterogeneous deformation within polycrystalline metals. To place this into context, the elastic range for most metals is within 10^{-3}, so most of the surface mapping analysis cannot be used to distinguish elastic strains but could be well suited to distinguish localized deformation.

2.5.2.2   Simulated Polycrystalline Deformation

Results from the FFT polycrystalline simulation are given in the first column of Figure 7, where the non-uniform maps for in-plane strain components, ε_{xx}, ε_{yy}, ε_{xy}, are shown. The middle column shows the corresponding in-plane strain maps as measured from DIC analysis for pattern P4 with a subset window radius of ~25 µm, subset spacing of ~1 µm, and strain window width of ~5 µm. The imaging resolution of, $\lambda_I = 1.07\ \mu m/pixel$ and grain resolution of $\lambda_G = 0.005\ grains/pixel$ means that this subset window diameter occupies ~1/4 the size of each grain. Pattern P4 is selected for viewing given its performance in the RBT analysis.   The third column shows the absolute difference between the simulation and DIC strain, for axial, transverse and shear components, at each image coordinate, x, as defined in Equation 11. As shown in the middle and right column of Figure 6, DIC is able to reproduce the heterogeneous strain fields quite well, and at most locations the difference between DIC measurements and simulated (true) strain is at least one order of magnitude smaller than true strain. This is

22

not true, however, at locations where strain is highly localized, such as near the grain boundaries of the polycrystalline material. At these locations deviation in measured strain tends to exceed 4×10^{-3}, which is much greater than the RBT estimated error.
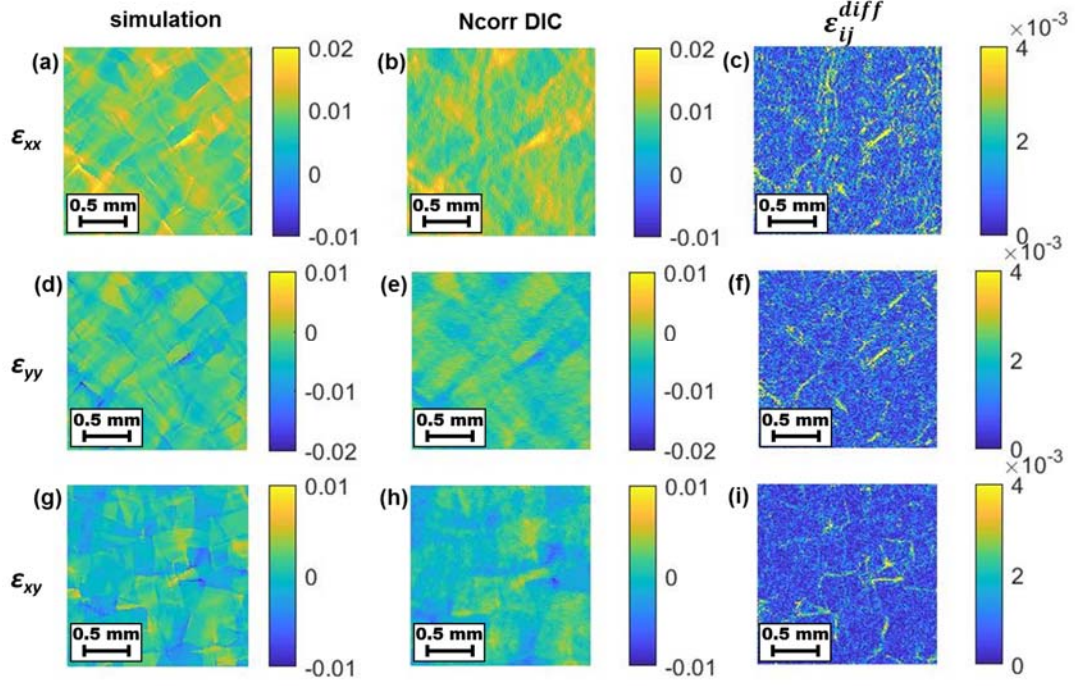
Figure 7. In plane strains (ε_{xx}, ε_{yy}, ε_{xy}) from numerical simulation (first column), calculated DIC strains (middle column) using pattern P4 with a subset size window of ~25 μm. Absolute deviation between the simulation and DIC strains (last column).

Accuracy of DIC measurements relies on a proper selection of subset window size, and this dependency is presented in Figure 8 which shows the absolute difference per Equation 11, for patterns P4 axial (top row) and transverse (bottom row) component as the subset window size is increased. For the smallest subset window size, random noise appears to produce deviations with high magnitude (greater than 4×10^{-3}). As the subset radius increases from ~15 μm to ~25 μm, the random deviations are reduced and fewer points, mainly close to the grain boundaries, appear to have deviations with such

large magnitude. For the ~50 μm subset radius, there are high deviations near the grain boundaries to the extent that the microstructure of the material becomes apparent in the error map plot. There appears to be very little difference between P4 and P1 error map especially for the largest subset radius.
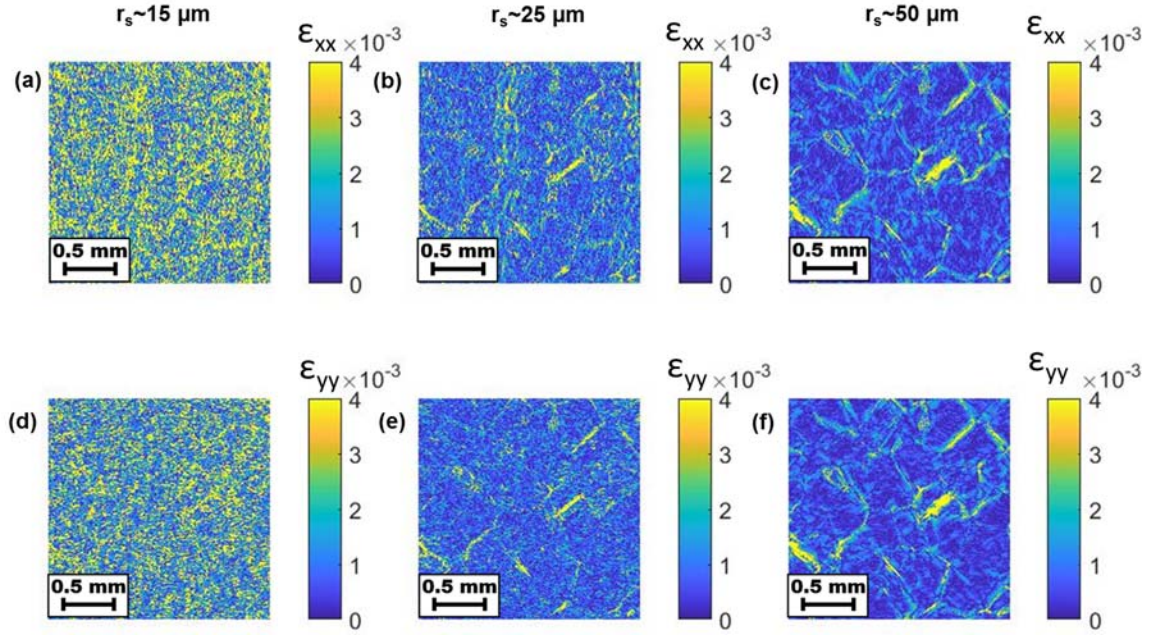
Figure 8. Absolute difference in the axial ε$_{xx}$ (top row) and ε$_{yy}$ (bottom row) strain components for pattern P4 for different subset window radii: ~15 μm, ~25 μm, and ~50 μm (first, second and third columns respectively).

The difference between DIC measured strain and true strain is more quantitatively analyzed in Figure 9, where the difference in DIC and simulation strains for the three in-plane strain components ε_{xx}, ε_{yy}, and ε_{xy} are plotted as a function of each respective true strain component's local magnitude for pattern P1 (top row) and P4 (bottom row). The local absolute difference is calculated for every voxel (using Equation 11), and the data is discretized into 10 evenly spaced bins between the minimum and maximum bounds of the independent variable studied on the x-axis, and the median deviation of each bin is

24

plotted. The shaded region represents the spread of data within one standard deviation from the median value. A careful selection of the maximum strain bin is accomplished by examining each strain map to determine the cut-off where high bins transition from meaningful information to isolated data points.
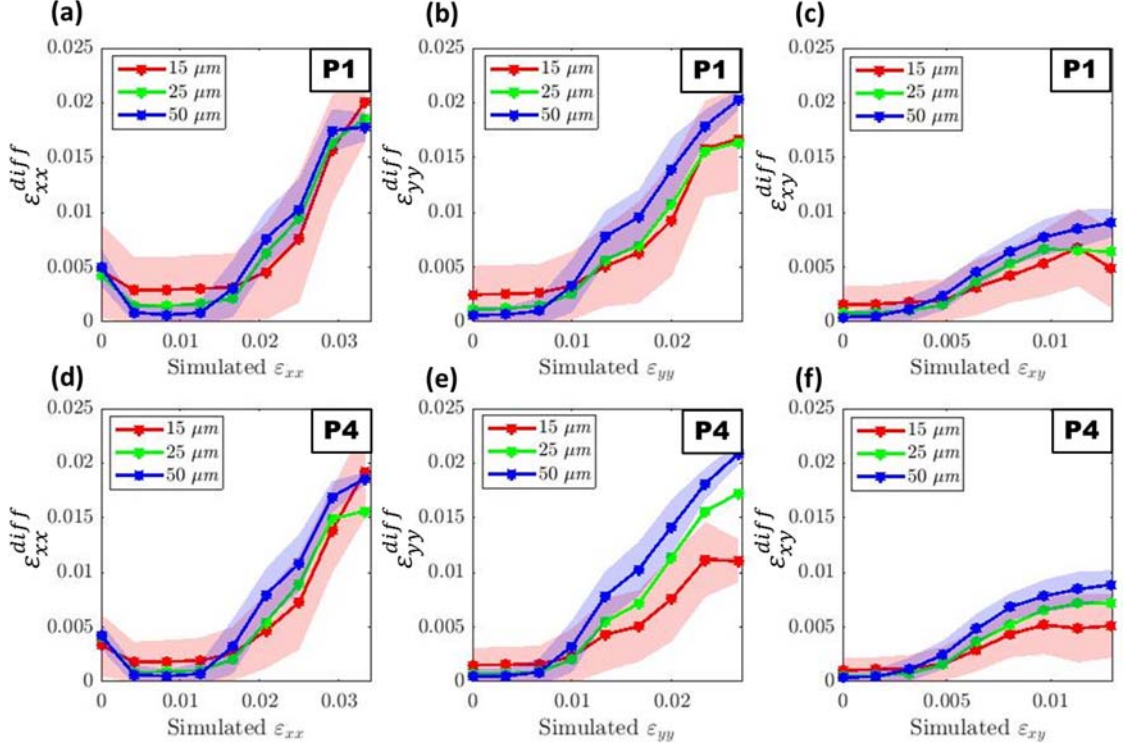
Figure 9. Absolute difference in strains between DIC and simulation as a function of simulated strains for P1 (top row) and P4 (bottom row).

In general, the deviation in strain as a function of simulation strain is nearly constant when the simulation strain is near macroscopic applied strain but rapidly grows when local simulation strains are greater than or less than the macroscopically applied strain. For example, near the 1% strain level, the deviation in ε_{xx} is nearly constant with a magnitude of 1.9×10^{-3} for P4 and 3.1×10^{-3} for P1 when the subset radius is ~15 μm, which is an order of magnitude smaller than the simulated strain. As the subset radius

25

increases from ~15 μm to ~50 μm the deviation in ε_{xx} reduces by a factor of 3 near 1%

strain. This trend of decreasing deviation with increasing subset radius is consistent with

the RBT analysis. The difference in strain deviation in ε_{xx} are 20% higher than the

numerical RBT error for P1 with 15 μm window radius and 4 times smaller for P1 with

50 μm radius. Away from the macroscopic strain level, the deviation substantially

increases for all strain components, rapidly approaching the same order as the simulated

strain levels. In the case of ε_{xx}, the deviation for P1 for 15 μm radius is ~3 times smaller

than the simulated strain of 2% and only 2 times smaller than the simulated strain of 3%.

Moreover, above the 1% strain, in regions of higher strain gradients the smaller window

radii tend to produce the least error. Deviation in ε_{xx}, at 2% simulated strain is $4.2 \times$

10^{-3} for P1 with 15 μm radius and increases by 70% to 7.2×10^{-3} for P1 when the

subset radius is 50 μm. Qualitatively from Figure 7, it could be seen that higher strain

levels tend to occur near regions of highly localized strain gradient. Averaging across a

larger window would certainly "blur" these high gradient areas more than a smaller

window would.

The above analysis is similar for other strain components and imply the same

conclusion: where strains are near average and their variations are low (for instance, at

locations well within grains) the difference between DIC measurements and true data is

reduced to within a reasonable margin, nearly an order of magnitude smaller than applied

strains depending on pattern quality, and best captured with a large subset window.

However, where strains vary greatly and have magnitudes much higher or lower than

average (likely at grain boundary locations) DIC measurements incur a much larger

deviation from true data, and a higher quality pattern must be used reduce this

uncertainty. Additionally, at locations with such localized deformation gradient, DIC results are most accurate when using a smaller subset window.

From Figure 9, a quantitative link between RBT analysis and polycrystalline deformation can also be established. This is accomplished by examining the DIC deviations in transverse and shear strain components at their mean location (where low strain and minimal variation best replicate RBT conditions). As the subset window increases from ~15, to ~25, and ~50 μm in radius, deviation in transverse strain measurements decrease from 2.3×10^{-3}, to 1.1×10^{-3}, and 5.2×10^{-3} for P1 and 1.4×10^{-3}, to 6.3×10^{-3}, and 4.1×10^{-3} for P4. For shear measurements, deviations decrease from 1.5×10^{-3}, to 7.1×10^{-3}, and 3.8×10^{-3} for P1 and 9.8×10^{-3}, to 4.5×10^{-3}, and 3.0×10^{-3} for P4, as the subset window is increased. Note that these values were obtained by increasing the number of bins so that a more accurate DIC deviation near mean strain could be examined. When compared to numerical RBT data, these values are consistently within 13% of the ~15 and ~25 μm radius subset window data, and well within the same order of magnitude for the ~50 μm data. This shows that RBT can indeed provide an expected baseline deviation for a pattern under low strain and low gradient conditions.

2.5.3   Uncertainty Analysis from Image Interpolation

The deformed pattern images studied in this work, for numerical RBT and polycrystalline deformation analysis, were obtained by digitally transforming the reference images using simulation deformation fields u and v, according to the following equation:

$$I'_{im}(\tilde{x}, \tilde{y}) = I_{im}(x, y), \tag{12}$$

where I'_{im} is the deformed image, I_{im} is the reference image, and $\tilde{x}$ and $\tilde{y}$ are as follows:

$$\tilde{x} = x + u(x, y), \tag{13}$$

$$\tilde{y} = y + v(x, y). \tag{14}$$

Interpolation is accomplished using a two-step procedure:

1. The deformation field from simulations is interpolated onto a grid corresponding to the resolution of the reference image. This is accomplished by assuming a certain length-scale for the simulation domain, which in this case is gathered from the average grain size of the microstructure.

2. The reference image is interpolated from a set of points $(\tilde{x}, \tilde{y})$ defined by Equations 13 and 14, to a regular grid (x, y). Interpolation is performed using the interp2 function provided by MATLAB, using PCHIP (Piecewise Cubic Hermite Interpolation Polynomial).

In order to quantify the uncertainty resulting from interpolation, an additional analysis was preformed of synthetic patterns, which could be deformed exactly according to a prescribed field. Since the interpolated simulation displacement fields could be considered a prescribed mapping of arbitrary resolution, focus is on quantifying the uncertainty resulting from step 2 of the interpolation procedure.

The synthetic pattern was generated as a collection of randomly place Gaussian speckles, given by the formula:

$$I_{im,\text{syn}} = \sum_{\tilde{p}} G_s(x - x_{\tilde{p}}^0, y - y_{\tilde{p}}^0), \tag{15}$$

where G_s is given by:

$$G_s = \exp\left(\frac{-(x^2 + y^2)}{d_s^2}\right), \tag{16}$$

and x_p^0 and y_p^0 are the coordinates of speckle $\tilde{p}$, and d_s is characteristic length scale chosen to be close that that in patterns described in Section 2.5.1. Since here the reference image is given by an analytical function, it can be deformed "exactly" (in a numerical sense) under a given displacement field. Figure 10 shows the synthetic pattern used in the tests. The strain fields obtained by DIC analysis from interpolated and "exactly" deformed images are compared in Figure 11. It can be readily seen that the difference between the two fields is within the noise level of DIC analysis. Thus it is concluded that the interpolation procedure does not introduce significant additional errors in the analysis.
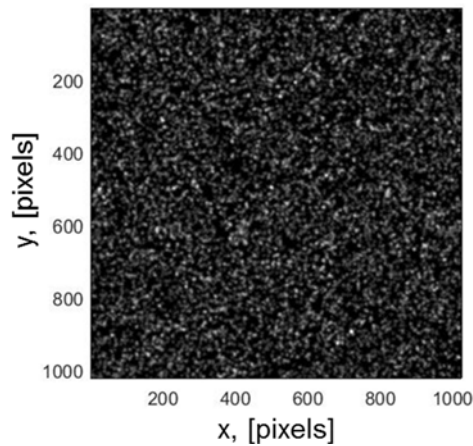
Figure 10. Synthetic image used for uncertainty analysis.
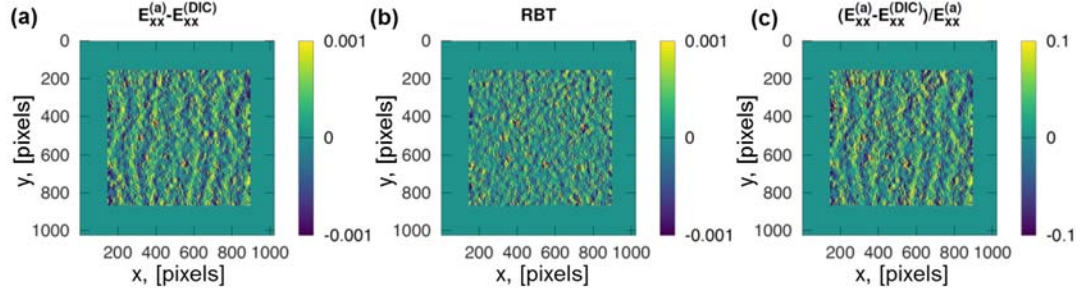
Figure 11. (a) Difference between DIC strains from analytically shifted and interpolated image, (b) strain field obtained from analytically shifted pattern, (c) relative error in DIC measurements between interpolated and analytically shifted image.

2.6   Instrument Resolution of Digital Image Correlation

At this point it has been demonstrated that the difference in DIC strains and simulations depends on the local strain magnitude. To determine an instrument resolution of DIC, based on pattern quality and subset selection, it is useful to fit a trend to the data presented in Figure 9 for the difference in strain between DIC and simulation as a function of simulation strain. Considering the previous discussion on where these deviations are minimized, and to what magnitude, several terms are predetermined to inform this curve-fitting. First, it was shown that deviation in strain measurements is constant, when local strains are close to the macroscopically applied strain. Second, at average applied strain this deviation is very close to numerical RBT analysis predictions. With these points in mind, the following equation is proposed:

$$\Delta_{ij}\left(\varepsilon_{ij}^{sim}\right) = \langle\varepsilon_{ij}\rangle_{RBT} + c_1\left(1 + \text{erf}\left(\frac{\left|\varepsilon_{ij}^{sim} - \bar{\varepsilon}_{ij}^{sim}\right| - \left(\bar{\varepsilon}_{ij}^{sim} + c_2\right)}{c_3 \cdot \bar{\varepsilon}_{ij}^{sim}}\right)\right) \tag{17}$$

where Δ_{ij} is the deviation, between true strain and DIC-measured strain, $\langle \varepsilon_{ij} \rangle_{RBT}$ is the difference in strains from numerical RBT analysis, $\bar{\varepsilon}_{ij}^{sim}$ is the average strain applied, c_1 is a constant governing range in deviation, and c_2 and c_3 are constants governing the variance in DIC measurement deviation in relation to average strain. Constants c_1, c_2, and c_3 are dependent on the pattern quality and subset window size selection. Essentially, Equation 17 enforces a cumulative density function that is symmetric about the location of applied strain. The constants determined for pattern P1 and P4, for the axial strain component, ε_{xx}, using each subset window size, are listed in Table 2.

Table 2. DIC resolution constants a and b for P1 and P4

Pattern	Subset Radius	c_1	c_2	c_3
P1	~15 μm	1.04×10^{-2}	7.88×10^{-3}	7.41×10^{-1}
	~25 μm	9.46×10^{-3}	5.08×10^{-3}	7.77×10^{-1}
	~50 μm	9.26×10^{-3}	3.32×10^{-3}	7.73×10^{-1}
P4	~15 μm	1.29×10^{-2}	9.80×10^{-3}	9.89×10^{-1}
	~25 μm	7.90×10^{-3}	3.87×10^{-3}	7.15×10^{-1}
	~50 μm	9.72×10^{-3}	3.64×10^{-3}	8.07×10^{-1}

Figure 12 shows the proposed fit to the DIC deviations shown in Figure 9. The fit is the solid line, and the data points represent the median of the difference in strain between simulation and DIC for each of the 10 bins.
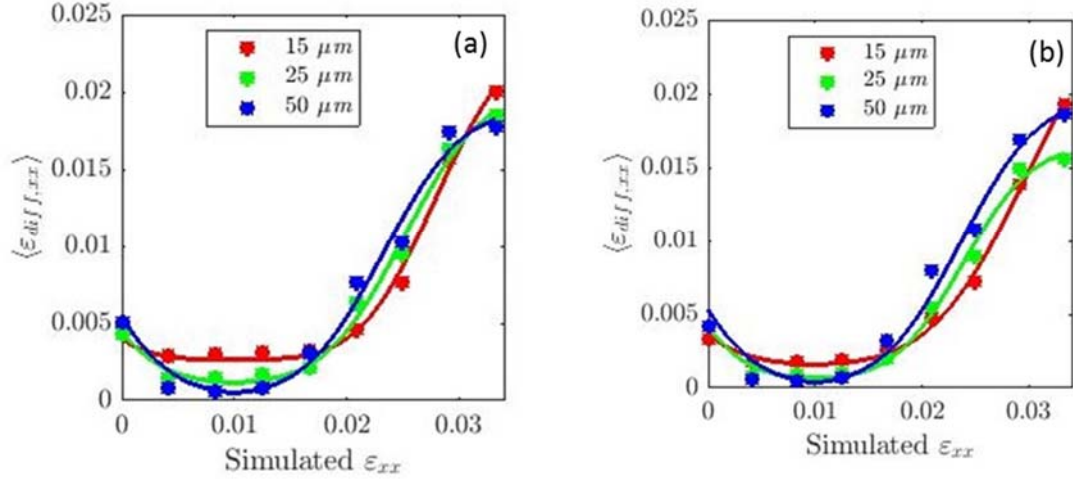
Figure 12. Data fit to the medians of the strain error for different subset window sizes for pattern (a) P1 and (b) P4.

From Figure 12, it can be seen that Equation 17 provides a very good fit to the accuracy in DIC measurements, essentially giving an instrument resolution in DIC based on pattern quality and subset window selection. Based on the material system of study, and expected strain gradients, one can use the data provided here to adjust and improve their DIC process so that strains are captured with the greatest accuracy. This information could assist in measuring strains across many different levels of the mesoscale, in turn validating physics-based numerical models with a well-predicted level of accuracy.

2.7   Summary and Conclusions

In summary, this chapter examined the accuracy of strain measurements in polycrystalline materials using DIC. Random patterns were generated using airbrush on a metallic surface. Patterns were characterized and both experimental and numerical RBT datasets were analyzed to obtain a baseline of the deviation from true strains. Images of each pattern were deformed according to a polycrystalline simulation. The deviations in

the strain fields from DIC were compared with those of the numerical polycrystalline simulations. The conclusions of the work are as follows:

1. Two point correlation and cluster analyses of patterns highlight features desirable in high quality patterns. For example, suitable patterns appear to have a rapid correlation function descent with a balanced area fraction. Cluster analysis indicates that a high population of finely dispersed, randomly arranged, closely spaced speckles is favorable.

2. Experimental and numerical RBT analyses suggest that the baseline deviation between DIC measurements and true data is substantially reduced when a larger subset window radius is used.

3. Since there are substantial deformation gradients in polycrystalline metals, subsequent analysis of the deviation in DIC measurements reveals that within a certain range, where local strains are near average bulk magnitude and local variations are low, DIC measurements will match RBT results and have greater accuracy as the subset window size is increased. For strains far from the mean value however, the opposite is true and error rapidly increases as subset window radius increases.

4. Finally, an instrument resolution for DIC was established, which is based on pattern quality and subset window size. This allows one to optimize their DIC process based on strain gradients which are expected in the material, and produce heterogeneous strain fields with improved accuracy.

In conclusion, recent works, e.g. [25], have demonstrated the weakness of using solely macroscopic load displacement curves in model calibration, where several

parameters cannot be uniquely defined. The work presented here can be used to calibrate models with reliable mesoscopic data, in the form of experimentally obtained deformation maps that have reasonable and predictable levels of uncertainty. Considering that microstructure evolution is an important ingredient in calibrating models, the integration of simulations and experiments at an early stage in the design cycle can allow us to extract quantitative information that has not been typically available.

CHAPTER 3.   USING EXPERIMENTAL IN-PLANE STRAIN MAPS TO CALIBRATE HIGHER ORDER NUMERICAL MODELS

3.1   Abstract

In this chapter, a physics-based polycrystalline plasticity model, originally proposed by Wen et al. [26], is described and employed in a finite element framework to simulate a uniaxial tensile test of a Grade 91 Fe-9Cr-1Mo alloy. The constitutive law explicitly describes the mobility of dislocations via glide and climb mechanisms, the effect on latent hardening, and the distribution of internal stresses at the sub-material point level. The influence of microstructural features, precipitates, grain and sub-grain boundaries, on material response is also accounted for in the constitutive law. The model is parameterized against an experimental load-displacement curve, where it is shown that an adequate fitting to experimental data can be accomplished using several, therefore non-unique, parameter combinations. With consideration to the uncertainty levels described in Chapter 2, the role of digital image correlation (DIC) in further reducing the parameter space is investigated, through an examination of the heterogeneous strain responses from the finite element simulation.

3.2   Background and Motivation

Over the past several decades, a large body of work has focused on deriving mechanistically based constitutive models that can simultaneously predict microstructure evolution and mechanical response of metals with varying crystal structure, texture, grain

size distribution, etc. [27, 28]. These complex models typically rely on crystal plasticity formulations and describe the effective contribution of each dissipative process activated during deformation that typically depends on the system's microstructure (i.e. grain size, precipitates, lathe phase etc.). Naturally, the number of calibration parameters increases with the number of deformation modes considered; such that model validation and parameterization is increasingly becoming more difficult. Despite challenges, such mechanistically founded models, as opposed to empirical fits, are expected to improve understanding of plasticity and accelerate material design.
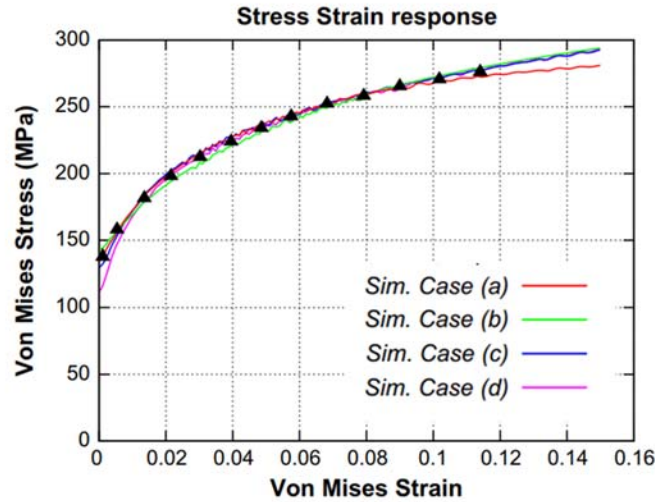
Figure 13. Matching stress-strain response from simulation [25], using different descriptions (a-d) of dislocation interaction hardening.

A common discrepancy with such high-order numerical models is the difficulty in determining the unique set of parameters that mathematically govern the material response. Indeed, it was shown by Bertin et al. [25] that several different combinations of parameters, which describe theoretically different dislocation interaction hardening modes, could give the same stress-strain response in their numerical simulations. These

matching bulk-outputs are shown in Figure 13. For the case of [25], clearly dislocation mobility has not been uniquely described and therefore this model cannot be expected to perform accurately outside of the conditions of the current validation.

Further bulk scale calibration can perhaps aid in the reduction of the parameter set, but this assumes access to a wide range of experimental test data (stress-strain, creep, fatigue, etc.) for many different environments. Perhaps more efficient would be the calibration of these terms on lower length scales. Given the minimized uncertainty presented in Chapter 2, this chapter aims to demonstrate this potential for lower length scale validation, using in-plane strain maps measured using DIC.

3.3 Numerical Modeling

3.3.1 Microstructure

The microstructural makeup of the Grade 91 steel alloy, studied in this chapter, leads to a complex series of interactions which will greatly contribute to hardening across the polycrystalline network. As such, it is important that these features are described, and their effects accounted for. The thermomechanical forming/processing of the alloy produces a stable martensite lath microstructure within packets (sub-grains), which make up the prior austenite grain boundaries. A high initial content of dislocations is found within grains after forming processes, and their mobility and interactions during loading will lead to hardening within grains and at sub-grain boundaries where they are arrested. Further, second-phase particles which result from the forming process, namely $M_{23}C_6$ (M = Cr) carbides and MX (M = V or Nb, X = C or N) precipitates, will obstruct the motion of dislocations. The $M_{23}C_6$ carbides lie mostly along sub-grain boundaries, and as a result

they prevent dislocation annihilation along these cell walls, which helps stabilize and slow the growth of sub-grains. MX precipitates will hinder the motion of dislocations within sub-grains. By limiting the flow of dislocations, both particle types will lead to a combined, enhanced hardening [29].

As suggested in Ashby's deformation map [30], the main mechanism of creep deformation can be determined by the temperature and stress state experienced in the material matrix. In high temperature conditions, diffusional flow driven by vacancy formation and migration, will dominate the creep behavior. At lower temperatures and higher stresses, dislocation flow and interactions will dominate the creep behavior. While a dominant creep mechanism can be discerned based on the environment, regimes will often occur simultaneously and therefore both must be accounted for.

3.3.2   Constitutive Law

The constitutive law considered here is the same as from Wen et al. [26], and considers the effects of dissipative processes of several different length scales, which are homogenized when appropriate. Dislocation mobility, precipitate interactions, and the resultant effects on latent hardening are explicitly described in a physical manner on the local material point scale. Those equations which are synonymous to ones from the FFT model in Section 2.4.1 will be rewritten here for ease of discussion.

3.3.2.1   Crystal Plasticity Model

The plastic strain rate at a material point is defined as the sum of all slip rates, multiplied by their orientation with respect to normal axes, as follows:

$$\dot{\varepsilon}_{ij}^{p} = \sum_{s} m_{ij}^{s}\, \bar{\dot{\gamma}}^{s}, \tag{18}$$

where $\dot{\varepsilon}_{ij}^{p}$ is the local plastic strain rate, $\bar{\dot{\gamma}}^{s}$ is the mean slip rate of a slip system s, and m_{ij}^{s} is the Schmid tensor, which is written symmetrically:

$$m_{ij}^{s} = \frac{1}{2}\left(n_i^s b_j^s + n_j^s b_i^s\right), \tag{19}$$

where $\mathbf{n}^s$ is the normal vector of the slip system, and $\mathbf{b}^s$ is the Burgers vector. Wang et al. [7, 31] consider the mean slip rate at a material point as the sum of the slip rates at sub-material points, each weighted by their volume fraction. The relationship is depicted by following:

$$\bar{\dot{\gamma}}^{s} = \int_{-\infty}^{\infty} \dot{\gamma}^{s}(\tau^{s}) P(\tau^{s} - \bar{\tau}^{s}) d\tau^{s}, \tag{20}$$

where $\dot{\gamma}^s$ is the slip rate at a sub-material point, which is a function of the resolved shear stress at each sub-material point, τ^s, and P is the probability distribution function that gives volumetric weight to each sub-material point, which is a function of the resolved shear stress and the mean resolved shear stress at a material point, $\bar{\tau}^s$. The mean resolved shear stress is determined simply by the tensor product of the local Cauchy stress tensor, $\boldsymbol{\sigma}$ and Schmid tensor at a material point:

$$\bar{\tau}^{s} = \boldsymbol{\sigma} : \mathbf{m}^{s}. \tag{21}$$

P can be written as a normal distribution centered about the mean resolved shear stress at a material point, with variance V_P as follows:

$$P(\tau^s - \bar{\tau}^s) = \frac{1}{\sqrt{2\pi V_P}} \exp\left(-\frac{(\tau^s - \bar{\tau}^s)^2}{2V_P}\right).$$ (22)

The slip rate is described by Orowan's equation, which is based on dislocation density, ρ_{cell}^s, Burgers vector magnitude, b, and the mean velocity of dislocations on the slip system, v, with sign determined by mean resolved shear stress as follows:

$$\dot{\gamma}^s = \rho_{\text{cell}}^s b v^s \cdot \text{sign}(\bar{\tau}^s)$$ (23)

3.3.2.2 Dislocation Mobility

The mean velocity of a dislocation depends on λ^s, the mean-free path between obstacles, and t^s, the duration that a dislocation spends between them. This relationship is defined on each slip system, and given in the following equation:

$$v = \frac{\lambda^s}{t^s}.$$ (24)

The two main obstacles considered are MX precipitates and other dislocations. Their aggregate effect on total mean-free spacing is given in the following equation:

$$\lambda^s = \left(\frac{1}{\lambda_{\rho,\text{cell}}^s} + \frac{1}{\lambda_{\text{MX}}^s}\right)^{-1}$$ (25)

where $\lambda^s_{\rho,\text{cell}}$ and λ^s_{MX} are the mean-free paths between dislocations and MX precipitates, respectively. The mean-free path between dislocations can be considered inversely proportional to the dislocation hardening within grains. Latent hardening from dislocations is due to interactions between dislocations among different slip planes and will evolve based on the present dislocation density at a material point [32]. The effect of dislocation self-interactions on latent hardening within the cell can described by the following relationship:

$$\tau^s_{\rho,\text{cell}} = \mu b \sqrt{\sum_{s'} \alpha^{ss'} \rho^{s'}_{\text{cell}}} \tag{26}$$

where $\alpha^{ss'}$ is the effective latent hardening matrix, which varies depending on whether or not dislocation interactions are collinear $(s = s')$. This expression proposed in [32] has been shown statistically accurate by discrete dislocation dynamic simulations [25]. The mean-free path between dislocations is therefore given by:

$$\lambda^s_{\rho,\text{cell}} = \frac{\mu b}{\tau^s_{\rho,\text{cell}}} \tag{27}$$

Spacing between MX precipitates is given by [33-35]:

$$\lambda^s_{\text{MX}} = h_{\text{MX}} \sqrt{\tilde{n}_{\text{MX}} d_{\text{MX}}} \tag{28}$$

where $\tilde{n}_{\text{MX}}$ is the number density of MX precipitates, d_{MX} is their average size, and h_{MX} is the trapping coefficient for a precipitate.

The duration that a dislocation spends between obstacles is the sum of the time spent waiting at an obstacle, t_w^s, and the time spent actually traveling between obstacles, t_t^s, [36-38]:

$$t^s = t_w^s + t_t^s \tag{29}$$

The time spent travelling between obstacles is short and can be approximated by assuming travel velocity is equal to the shear wave velocity, C_s, given below [39, 40]:

$$C_s = \sqrt{\frac{\mu}{\rho_0}}, \tag{30}$$

where μ is the shear modulus, and ρ_0 is the mass density of the material. Therefore travel time is given by:

$$t_t^s = \frac{\lambda^s}{C_s} \tag{31}$$

The waiting time will depend on which type of obstacle is encountered, either another dislocation or a precipitate, and therefore is the dependent upon the following equation:

$$t_w^s = P_\rho t_{w,\rho}^s + P_{MX} t_{w,MX}^s \tag{32}$$

where P_ρ and P_{MX} are the probabilities of encountering another dislocation and MX precipitate, respectively, and $t_{w,\rho}^s$ and $t_{w,MX}^s$ are the waiting times associated with each obstacle. Note that since dislocations and MX are the only obstacles considered in this

context: $P_{MX} = 1 - P_\rho$. The probability of encountering either another dislocation or MX precipitate can be determined by the ratio of an obstacle's mean free spacing with the total interspacing from Equation 25. The probability of encountering another dislocation is therefore given by the following:

$$P_\rho = \frac{\lambda^s}{\lambda^s_{rho,cell}} = \frac{\sqrt{\sum_{s'} \alpha^{ss'} \rho^{s'}_{cell}}}{\sqrt{\sum_{s'} \alpha^{ss'} \rho^{s'}_{cell}} + h_{MX}\sqrt{N_{MX}d_{MX}}} \tag{33}$$

The time which a dislocation spends waiting at each obstacle is determined by the time it spends scaling the obstacle via either a dislocation climb process, t_c, or glide process, t_g, which can occur simultaneous to one another. The time spent for each process can be summed to give the total waiting time as follows:

$$t_{w,i} = \left(\frac{1}{t_{g,i}} + \frac{1}{t_{c,i}}\right)^{-1} \tag{34}$$

where i denotes the obstacle type; ρ or MX.

The dislocation glide process here refers to obstacle bypass via junction unzipping and the Orowan mechanism for dislocation bowing around large particles. These processes are considered thermally activated and therefore their waiting times can be described by the Kocks-type enthalpy activation law [37, 39, 41]:

$$t_{w,g} = \frac{\exp\left(\frac{\Delta G^s_i}{kT}\right)}{v^s_{G,i}} \tag{35}$$

where ΔG_i^S is the activation energy, k is the Boltzmann constant, T is absolute temperature, and $\nu_{G,i}^S$ is the effective attempt frequency for overcoming an MX precipitate. The attempt frequency is assumed constant, and is considered equal to the travelling velocity, C_s, divided by the length of vibrating dislocation segments, λ^s, multiplied by an entropy factor, χ [7, 42],

$$\nu_{G,i} = \frac{\chi C_s}{\lambda^s}.$$

(36)

The activation energy depends on the ratio of resolved shear stress to critical resolved shear stress, τ_c^S, and is given below:

$$\Delta G_i^S = \begin{cases} \Delta G_{0,i} \left(1 - \left(\frac{\tau^s}{\tau_c^s} \right)^p \right)^q & \text{if } \tau^s < \tau_c^s \\ 0 & \text{if } \tau^s \geq \tau_c^s \end{cases}$$

(37)

where $\Delta G_{0,i}$ is the activation energy in the absence of any applied stress, and p and q are empirical terms which govern the stress dependence.

The critical shear stress on each slip system evolves over time based on contributions from different latent hardening mechanisms. Hardening effects from different sources can be added in superposition, in the following form:

$$\tau_t^m = \sum_i \tau_i^m$$

(38)

where i denotes the hardening source, m is an exponent for combining hardening sources, and τ_t is the total combined hardening from all processes. In this work, hardening effects from dislocation self-interactions and from the presence of precipitates are considered.

Overall hardening due to dislocation self-interactions, τ_ρ^s, is similar to Equation 26 but with dislocation density at the cell wall, ρ_{cw}, also included:

$$\tau_\rho^s = \mu b \sqrt{\sum_{s'} \alpha^{ss'}\left(\rho_{\text{cell}}^{s'} + \rho_{\text{cw}}^{s'}\right)}. \tag{39}$$

Hardening effects from MX and M$_{23}$C$_6$ precipitates are lumped together in this work, and given by τ_P^s. Therefore, using Equation 38, overall critical resolved shear stress is given by the following equation,

$$\tau_c^s = \tau_0^s + \left[\left(\tau_\rho^s\right)^m + (\tau_P^s)^m\right]^{1/m} \tag{40}$$

where τ_0^s is an inherent frictional stress, which can be simply added to the overall hardening [35, 43, 44].

The dislocation climb process here refers to the ability of an edge dislocation to scale an obstacle, by means of point defect absorption and emission, in the direction perpendicular to its slip plane. The waiting time can be given by the magnitude of climb velocity, v_c^s, the distance a dislocation needs to climb to bypass an obstacle, l_i, and R_e [45] which is the proportion of dislocations that are edge dislocations:

45

$$t_{w,c,i} = \left(R_e \frac{|v_c^s|}{l_i} \right)^{-1} \tag{41}$$

For non-irradiated materials, the climb process is considered diffusion-controlled and can be described by a net vacancy flux through the gradient of vacancy concentration [46]. Climb velocity is given by:

$$v_c^s = \frac{I_v^s \Omega}{b} \tag{42}$$

where I_v^s is the net current of vacancies for a given slip system and Ω is the atomic volume. The net current vacancy is given in the following equation [40, 46-50]:

$$I_v^s = \frac{2\pi D_v \left[C_v^\infty - C_v^0 \exp\left(\frac{-f_c^s \Omega}{kTb} \right) \right]}{\Omega b \ln(r_\infty / r_d)} \tag{43}$$

where D_v is vacancy diffusivity within the grain volume, C_v^∞ is the equilibrium vacancy concentration of the material, C_v^0 is the current vacancy concentration (assumed equal to C_v^∞ in this model), f_c^s is the climb component of the Peach-Kohler force, r_d and r_∞ denote the inner and outer radii of the cylindrical control volume around the dislocation line. The climb component of the Peach-Kohler force can be computed from the dot product of the Peach-Kohler force, $\mathbf{f}_c$, with the unit normal of the slip plane:

$$f_c^s = \mathbf{f}_c \cdot \mathbf{n}^s \tag{44}$$

where the Peach-Kohler force is defined as follows [51-53]:

46

$$\mathbf{f}_c = [(\boldsymbol{\sigma} \cdot \mathbf{b}^s) \times \mathbf{t}^s]. \tag{45}$$

In the above equation, $\boldsymbol{\sigma}$ is the deviatoric stress tensor at a material point, and $\mathbf{t}^s$ is the unit tangent vector to the dislocation line, which is equal to the cross product of the normal and Burgers vector of a slip system [54, 55]:

$$\mathbf{t}^s = \mathbf{n}^s \times \mathbf{b}^s. \tag{46}$$

The equilibrium vacancy concentration is given by [46]:

$$C_v^0 = \exp\left(\frac{S_f^v}{k}\right)\exp\left(-\frac{E_f^v}{kT}\right) \tag{47}$$

where S_f^v and E_f^v are the vacancy formation enthalpy and energy, respectively. Expressions for vacancy formation terms and diffusivity, determined by the molecular dynamics simulations of Mendelev and Mishin [56], are given below:

$$E_f^v = g_0 - g_2 T^2 - 2g_3 T^3 \tag{48}$$

$$S_f^v = -g_1 - 2g_2 T - 3g_3 T^2 \tag{49}$$

where g_0, g_1, g_2, and g_3 are phenomenological coefficients governing the effect of temperature on vacancy formation. Diffusivity is calculated by:

$$D_v = D_0 \exp\left(-\frac{E_m^v}{kT}\right) \tag{50}$$

where D_0 is a diffusion constant, and E_m^v is the vacancy migration energy [56].

3.3.2.3 Dislocation Density Evolution

It can be seen in previous equations that dislocation density is important in governing the slip rate and the critical shear stress on each slip system. As such, it is necessary to incorporate the evolution of dislocation density within grains and at grain boundaries. The net change in dislocation density within in a sub-grain can be given by the sum of generated dislocations $\dot{\rho}_{\text{cell,gen}}^{s}$, minus those which have been annihilated, $\dot{\rho}_{\text{cell,ann}}^{s}$, and trapped at cell walls, $\dot{\rho}_{\text{cell,trap}}^{s}$:

$$\dot{\rho}_{\text{cell}}^{s} = \dot{\rho}_{\text{cell,gen}}^{s} - \dot{\rho}_{\text{cell,ann}}^{s} - \dot{\rho}_{\text{cell,trap}}^{s}. \tag{51}$$

Dislocation generation is given by the typical expression for area swept by moving dislocations [57-59]:

$$\dot{\rho}_{\text{cell,gen}}^{s} = \frac{k_1}{b\lambda^s} |\bar{\dot{\gamma}}^s| \tag{52}$$

where k_1 is an empirical material constant for dislocation generation. Annihilation of dislocations is due to a collision of two dislocations with opposite Burgers vectors, mostly occurring during cross-slip and climb [60, 61]. This dynamic recovery can be written using Kocks-Mecking law [60, 62, 63]:

$$\dot{\rho}_{\text{cell,ann}}^{s} = f_e \rho_{\text{cell}}^{s} |\bar{\dot{\gamma}}^s| \tag{53}$$

where f_e is the recovery parameter, which Estrin concluded is mostly sensitive to the strain rate using the general expression below [60]:

$$f_e = k_2 \left(\frac{\dot{\varepsilon}_0}{\dot{\varepsilon}}\right)^{1/n_0} \tag{54}$$

where k_2 is a material constant, $\dot{\varepsilon}_0$ is a reference strain rate, and n_0 is a strain rate sensitivity parameter.

Dislocations will become immobilized after they have swept a certain area [34, 38, 64], which in the case of cell wall trapping can be considered the sub-grain size, λ_{sg}. The dislocation evolution change due to trapping at cell walls is therefore given by the following equation:

$$\dot{\rho}_{\text{cell,trap}}^S = \frac{k_3}{\lambda_{sg}}|\bar{\dot{\gamma}}^s| \tag{55}$$

where k_3 is a material constant. Dislocation density evolution at cell walls is given by the net effect of trapping at cell walls and the annihilation of dislocations within them, $\dot{\rho}_{\text{cell,ann}}^S$, given below:

$$\dot{\rho}_{\text{cw}}^S = \dot{\rho}_{\text{cell,trap}}^S - \dot{\rho}_{\text{cw,ann}}^S \tag{56}$$

Dislocations within the cell wall cannot glide [65]. Therefore annihilation of dislocations with opposing Burgers within cell walls must be due to climb, which Nes [61] proposed is proportional to dislocation climb velocity and dislocation density, and inversely proportional to average dipole separation, l_g. Additionally, average dipole separation is inversely proportional the square root of dislocation density in the cell wall.

Therefore the family of formulas which describe dislocation density evolution are as follows:

$$\dot{\rho}^s_{\text{cell,ann}} \propto \frac{\rho_{\text{cw}} |v_c^s|}{l_g} \tag{57}$$

$$l_g \propto \frac{1}{\sqrt{\rho_{\text{cw}}}} \tag{58}$$

$$\dot{\rho}^s_{\text{cell,ann}} = k_c |v_c^s| (\rho_{cw}^s)^{\frac{3}{2}} \tag{59}$$

where k_c is an empirical constant which quantifies the effects of dipole separation, dislocation density, and climb velocity.

3.4   Modeling Framework

3.4.1   Finite Element Modeling

The constitutive law compiled above is implemented in a finite element framework. This full-field approach allows for local material point description of each dissipative process defined in the model. Further, the polycrystalline microstructure (grain size, crystallographic orientation, etc.) is permitted to properly influence local material behavior. As with any finite element model, heterogeneous material response is outputted, which can be used to validate the model with experimental data on lower length scales and even provide further insight into local material reactions.

The finite element software used is FreeFem++ [66]. FreeFem++ is an open-source, partial differential equation solver, with enhanced functionality for finite element

framework formulation. The software allows the user to completely define the constitutive law, governing balance equation, and iterative problem description, all within a C++ style coding environment. Additionally, the software can be configured to solve using parallel processing, which allows for efficient operation in high performance computing (HPC) environments.

Within this framework, a thin plate made up of a 5x5 columnar grain structure was modelled with 499x499x1 grid of tetrahedral elements, using quadratic interpolations of displacement between nodes. The front of the polycrystalline structure considered is shown in Figure 14(a), and the cross-section showing the side-view is in Figure 14(b).
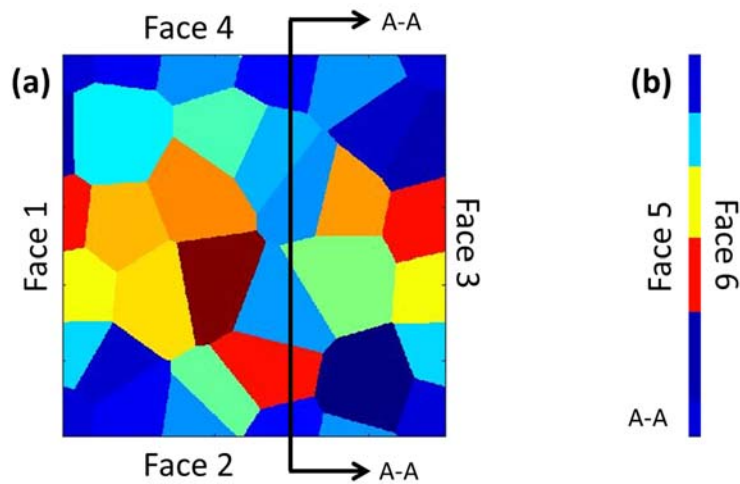
Figure 14. (a) Front view of polycrystalline structure from numerical model, (b) side-view of polycrystal.

To simulate uniaxial tension, for either increasing displacement (stress-strain testing) or constant load (creep testing), the boundary conditions given in Equation 60 were enforced. Zero displacement in the horizontal axis was prescribed for the left face of the plate, zero displacement in the vertical direction was prescribed for the top face, and

zero displacement in the out-of-plane direction was prescribed for the back face. For the case of load-displacement testing, a displacement on the right face was enforced, and increased over time according to an applied strain rate. For the case of creep, a two-dimensional surface integral of macroscopic stress traction was applied to the right face, and maintained at a constant magnitude throughout simulation.

$$\text{On face 1: } u_x = 0$$

$$\text{On face 3: } \begin{cases} u_x = u_{disp} & \text{(displacement input)} \\ \int_A \sigma_{ij} n_i dA & \text{(stress input)} \end{cases} \tag{60}$$

$$\text{On face 4: } u_y = 0$$

$$\text{On face 5: } u_z = 0$$

Considering Cauchy's first equation of motion, a balance equation can be used in variational form to solve for the local displacements of the model. Neglecting body forces and assuming the body is at equilibrium, the balance equation with plastic strain addition is given as follows, depending upon loading conditions:

$$\int_V [\boldsymbol{\varepsilon}(\tilde{u})\mathbf{C}\boldsymbol{\varepsilon}(u) + \boldsymbol{\varepsilon}(\tilde{u})\mathbf{C}\boldsymbol{\varepsilon}^p(u)]dV = 0 \tag{61}$$

$$\int_V [\boldsymbol{\varepsilon}(\tilde{u})\mathbf{C}\boldsymbol{\varepsilon}(u) + \boldsymbol{\varepsilon}(\tilde{u})\mathbf{C}\boldsymbol{\varepsilon}^p(u)]dV + \int_A \sigma_{ij} n_i dA = 0 \tag{62}$$

where **C** is the stiffness tensor, $\boldsymbol{\varepsilon}$ is the strain tensor, $\boldsymbol{\varepsilon}^p$ is the plastic strain tensor, u is the displacement, and $\tilde{u}$ is a virtual displacement. In the case of creep testing, Equation 62 is used in place of Equation 61.

The constitutive law is computed over time, which must be discretized into individual time steps. At the beginning of each time step, the balance law given in Equation 61, or 62, is solved giving local displacements at each mesh node. Local strains are calculated from a simple differentiation of displacements, as shown in Equation 63.

$$\varepsilon_{ij} = \frac{\partial u_i}{\partial x_j} \tag{63}$$

It is assumed that each time step strain increment is sufficiently small so that additive strain decomposition can be used to relate elastic and plastic strains to overall strain, as follows:

$$\varepsilon_{ij} = \varepsilon_{ij}^e + \varepsilon_{ij}^p \tag{64}$$

which allows solving for stresses from Hooke's Law in Equation 65 below:

$$\sigma_{ij} = C_{ijkl}\varepsilon_{kl}^e \tag{65}$$

The stresses at each node are used to solve for the resolved shear stress on each slip system, using Equation 21, and the remaining components of the constitutive law described above can be solved for directly to compute a final local plastic strain rate for the time step in Equation 18. The plastic strain rate is then added to overall plastic strain,

with respect to the time step interval, and the next iteration begins again with solving the balance equation.

3.4.2   *Computational Efficiency Efforts*

From the constitutive law description given in Section 3.3.2, it can be seen that implementation of the model within a finite-element framework requires a substantial number of calculations at each mesh node. As a result, it was found that high-resolution simulations were subject to total solve-times which were often several orders of magnitude longer than the experiments themselves. It is a given that numerical modelling efforts should be focused on reproducing experimental data both at lower cost and with greater efficiency, and as such, it was necessary to implement several strategies to reduce the overall run-time of the simulation. The two most important/effective efficiency strategies that were implemented are described here. While these methods are described specifically in the context of the present work, the general ideas presented can be applied almost ubiquitously to other modelling efforts. As future numerical models aim to describe more dissipative processes on different length scales, they will require more computations per iteration and therefore potentially longer run times and greater memory demands. As such, it is imperative that strategies, like the two presented herein, are utilized to reduce computation volume and make use of advancing computer technologies.

3.4.2.1   Parallel Architecture

First, the script describing the constitutive law and finite element framework was rewritten to solve in parallel, so that multiple processors could be used simultaneously to

compute local data, instead of computing in series. This entailed partitioning the finite element mesh into n number of regions, where n is the total number of processors being used to execute the simulation. Partitioning of meshes was accomplished using HPDDM, which distributed respective mesh domains to different processors, and METIS [67], a multilevel graph partitioning scheme optimized for finite element method. Each processor "owned" respective fractions of the mesh, and therefore only needed to compute local plastic strain rates at their own mesh nodes. To collect data from each processor and solve the overall balance equation, a linear PETSc [68] solver was used, which is designed to efficiently handle parallel, distributed arrays of data that are combined to compute partial differential equations.

This method of parallel computing was effective for the obvious reason that each processor was only responsible for $1/n$ fraction of total computations, and as such the overall run-time scaled by approximately this factor. Perhaps less obvious, is the benefit of having no "global" meshes or "master" processors. Since each processor exclusively knows its mesh data, the memory demand from each processor also scales by $1/n$, and total memory usage is always maintained. In earlier parallelization attempts the entire, "global," mesh was still defined on every processor, and as a result total memory demand would actually scale up by a factor n. Additionally, for very fine meshes, passing such high volumes of data between processors was simply not possible. So the current strategy, in addition to scaling down computation time by $1/n$, would scale memory usage per processor by this factor as well. Since the model was implemented in a HPC environment, where upwards of 100 total processors were often used, this meant significant time reduction in overall simulation run-time.

To give an idea of the reduction in solve time from using parallel processing, Figure 15 shows the decreasing iteration time for a low resolution mesh (49x49x1 elements) when the number of processors used is increased from 1 to 4. It can be seen that the assuming scaling of $1/n$ is observed, where iteration time reduces from approximately 54 seconds to 28 seconds, and eventually to 13 seconds when using 1, 2, and 4 processors respectively.
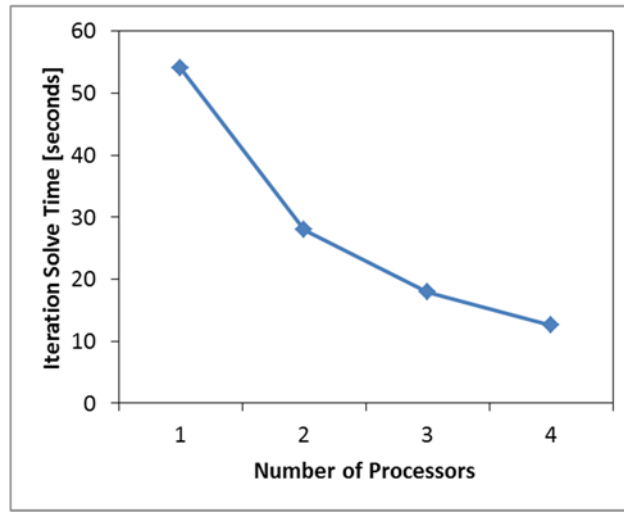
Figure 15. Iteration time-dependence on number of processors used in parallel.

3.4.2.2 Numerical Integration Scheme

Computation of the material point integral in Equation 20 required a numerical integration scheme, which here is based on a simple Riemann sum approximation of the integral:

$$\bar{\gamma}^s = \int_{-\infty}^{\infty} \dot{\gamma}^s P(\tau^s - \bar{\tau}^s) d\tau^s = \sum_i^{n_p} \frac{k_p}{n_p} \dot{\gamma_i}^s P_i(\tau^s - \bar{\tau}^s) \tag{66}$$

where k_p is the width of the Gaussian integration bin, and n_p is the number of integration points which are equally spaced between upper and lower bounds of the integral.

Certainly, the summation cannot be accomplished between the indefinite bounds described above, so an approximation of the upper and lower limits was used. The criterion chosen, for calculating the bounds of summation, was the minimum probability weight, from Equation 22, that would still be considered significant in calculating slip rate. This value, P_0, could be used to determine the maximum and minimum sub-material stress bounds for use in Equation 66, as follows:

$$\tau_b = \pm\sqrt{-2V log\left(P_0\sqrt{2\pi V_P}\right)} \tag{67}$$

where τ_b is the distance above and below mean stress, governing the range of numerical integration. For this work it was determined that any probability weight less that $P_0 = 1 \times 10^{-24}$ was negligible in calculating overall slip rate.

From here, the simplest approach would be to use a large number of integration points, so that mean slip rate can be calculated with the greatest accuracy. However, given that this slip rate is computed for each slip system, at every node, even a small difference of 10 integration points will add total 1.2×10^8 calculations per time-step for a high resolution mesh with 500x500x2 nodes. Therefore, limiting the number of integration points on each slip system, while maintaining reasonable accuracy, is greatly desired.

Several strategies were considered for approximating the Gauss integral. The simplest and most effective approach was to determine the minimum number of integration points necessary to compute slip rate within 0.1% accuracy. This minimum number of points was found to vary based on the difference between mean shear stress and critical shear stress on a slip system, and this relationship is plotted in Figure 16 below:
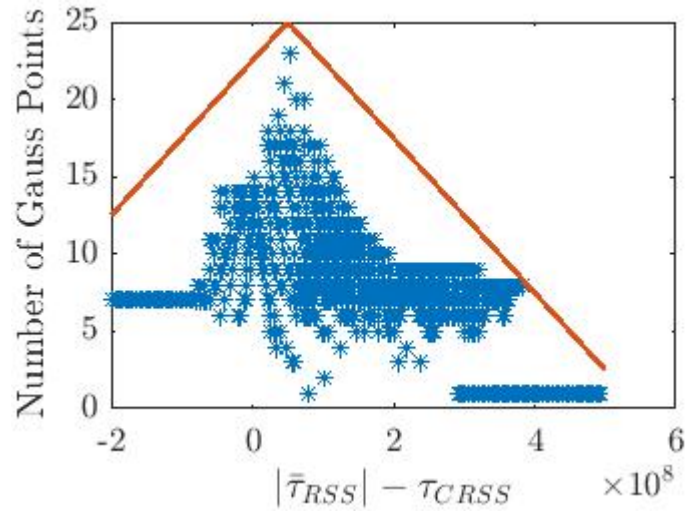
Figure 16. Minimum number of gauss points for slip rate calculation.

Blue asterisks in Figure 16 represent the minimum number of integration points required to determine slip rate with reasonable accuracy, for several different temperatures and stress-states. The red line in Figure 16 represents a simple (and conservative) approximation of this minimum, and is used to prescribe to the simulation the number of integration points to be used in calculating mean slip rate. This line can be described by the following formula:

$$n_p = |\tau_c^s - |\bar{\tau}^s| - 5 \times 10^{-7}| \cdot (-5 \times 10^{-8}) + 25 \tag{68}$$

where the number of integration points, n_p, is determined for use in Equation 66. Note that within the script itself, a minimum of five gauss are used when Equation 68 gives $n_p < 5$. From implementing this numerical integration approach, iteration times (and total solve time) were typically reduced by approximately half when using Equation 68 to define the number of integration points, compared to using a constant 25 points.

The iterative solve of the numerical simulation can be visualized in Figure 17:
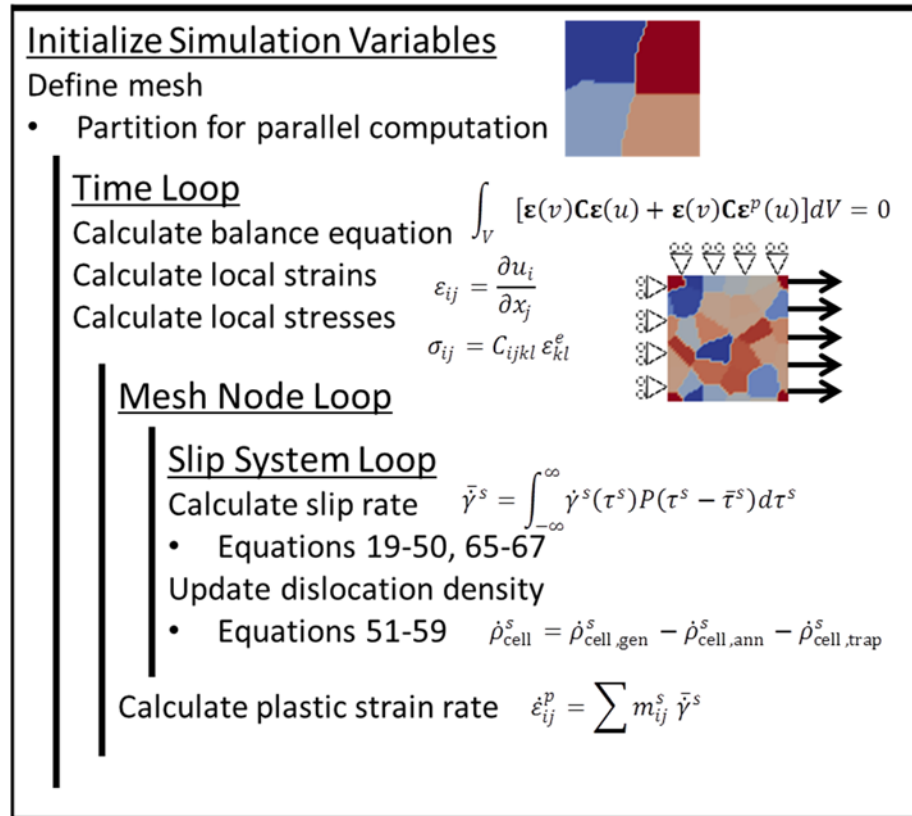
Figure 17. Iterative solve description of numerical simulation.

3.5   Model Validation and Discussion

3.5.1   Bulk Scale Validation

Calibration of a numerical model is often accomplished through a comparison of bulk responses between model and experimental data. In this work, the model compiled above is parameterized against an experimental load-displacement curve obtained from 0.3% s^{-1} strain rate loading of the Grade 91 FeCrMo alloy at 823K, from Dundulis et al. [69]. In the original model description, Wen et al. parameterized the constitutive law for the same material system against high temperature creep data, within a mean-field viscoplastic self-consistent framework. Most parameters can be maintained from the original, but slight adjustments are necessary to accommodate the full-field framework and slightly lower temperature state in the present work. Namely the variance, V, in sub-material stresses from Equation 22 is reduced by 10% to prevent constructive interference between neighboring finite element nodes, and the hardening from precipitates, τ_P^S, is increased since temperature is decreased. The entire list of parameters is shown in Table 3.

Table 3. Parameters for numerical simulation of FeCrMo alloy.

Parameter		Fe-Cr-Mo [26]
ρ_0	Mass density	8000 Kg/m^3
b	Magnitude of Burgers vector	$2.48 \times 10^{-10} \text{ m}$
μ	Shear modulus	103572 MPa $-\text{T} \cdot 48 \text{ MPa/K}$
$\tilde{n}_{\text{MX}}$	Number density of MX precipitates	$3 \times 10^{20} \text{m}^{-3}$
D_{MX}	Average diameter of MX precipitates	37 nm
h_{MX}	Trapping coefficient for MX precipitates	1
τ_0	Friction stress	0 MPa
τ_P^S	Hardening contribution of MX precipitates	390 MPa for 823 K 315 MPa for 973 K
m	Superposition hardening exponent	2
α^{ss}	Dislocation hardening from collinear interaction	0.05
$\alpha^{ss'}$	Dislocation hardening from non-collinear interaction	0.7
V	Variance of resolved shear stress at material point	1000 MPa^2
$\Delta G_{0,\rho}$	Zero-stress activation energy for dislocations	2.8 eV
$\Delta G_{0,\text{MX}}$	Zero-stress activation energy for MX precipitates	7 eV
p	Exponent parameter	0.7
q	Exponent parameter	1.4
$\nu_{G,\text{MX}}$	Attack frequency for MX precipitate obstacles	$1.2 \times 10^{10} \text{s}^{-1}$
R_e	Proportion of edge dislocations	10%
χ	Entropy factor	1
r_d	Inner radius of dislocation control volume	$4b$
r_∞	Outer radius of dislocation control volume	$200b$
$\rho_{\text{cell},0}^S$	Initial dislocation density within cells	4×10^{12}
$\rho_{\text{cw},0}^S$	Initial dislocation density at cell walls	1×10^{13}
l_p	Average dislocation climb distance	$100b$
k_1	Dislocation generation term	0.12
k_2	Dislocation annihilation term	85
k_3	Dislocation cell wall trapping term	0.5×10^9
k_c	Dislocation cell wall annihilation term	0.1
λ_{sg}	Sub-grain size	$0.5 \times 10^{-6} \text{ m}$
n_0	Annihilation strain-rate sensitivity exponent term	3.5
D_v^0	Diffusion constant	$7.87 \times 10^{-7} \text{ m}^2/\text{s}$
E_m^v	Vacancy migration energy	0.6 eV
g_0	Vacancy energy/entropy term	1.724 eV
g_1	Vacancy energy/entropy term	$-1.2 \times 10^{-4} \text{ } e\text{V/K}$
g_2	Vacancy energy/entropy term	$-2.79 \times 10^{-8} \text{ eV/K}$
g_3	Vacancy energy/entropy term	$-5.93 \times 10^{-11} \text{ eV/K}$
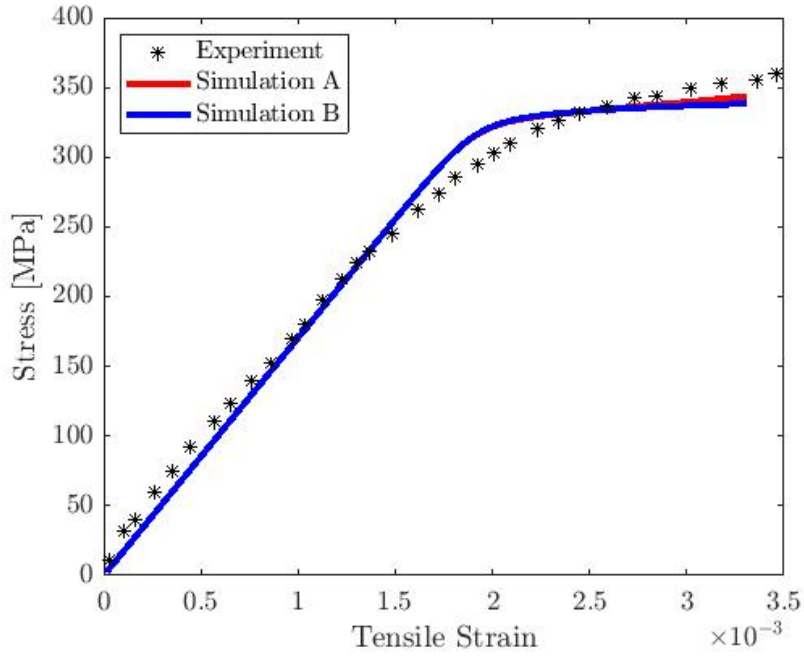
Figure 18. Stress strain curves from Simulations A and B and comparison with experimental data.

In their study of latent hardening due to dislocation self-interactions, Bertin et al. [25] briefly discussed the issue of non-unique parameter combinations with respect to bulk material response. Specifically the authors showed that different combinations of parameters for dislocation density generation, k_1, and frictional stress, τ_0, could produce the same bulk response despite theoretically describing different hardening modes. This issue is recreated using the present constitutive law, where dislocation generation and annihilation terms k_1 and k_2 can be varied by several orders of magnitude from Table 3 values, and yet still produce matching stress-strain curves. These terms, k_1 and k_2, govern the evolution of dislocation density within the sub-grains, which directly contributes to latent hardening within the material based on the equations presented above. Specifically, k_1 gives weight to the effect of the local mean slip rate on the

accumulation of mobile dislocations, while k_2 gives weight to the effect of local strain rate on dislocation recovery. The relationship between these two terms drives overall hardening, and by simply comparing the slope of hardening in an experimental stress-strain curve to a simulation, one can fit the ratio of these terms, that is: k_1/k_2.

Matching outputs from two extremes of dislocation evolution description are shown in Figure 18, alongside experimental data from Dundulis et al. [69]. The dislocation density evolution terms used to produce each simulation are shown in Table 4.

Table 4. Varied dislocation generation and annihilation terms.

	k_1	k_2
Simulation A	1.2×10^{-4}	0.15
Simulation B	0.12	150

Both bulk responses might be considered "valid" against the experimental data, and only vary from each other by a maximum of 2%, but an examination of either simulation's sub-grain dislocation density as a function of applied tensile strain in Figure 19 shows that on the mesoscale, two different phenomena are exhibited. Dislocation density in Simulation A rapidly decreases compared to Simulation B, and even after a relatively small amount of strain there exists a 14% difference in dislocation population between simulations.

63
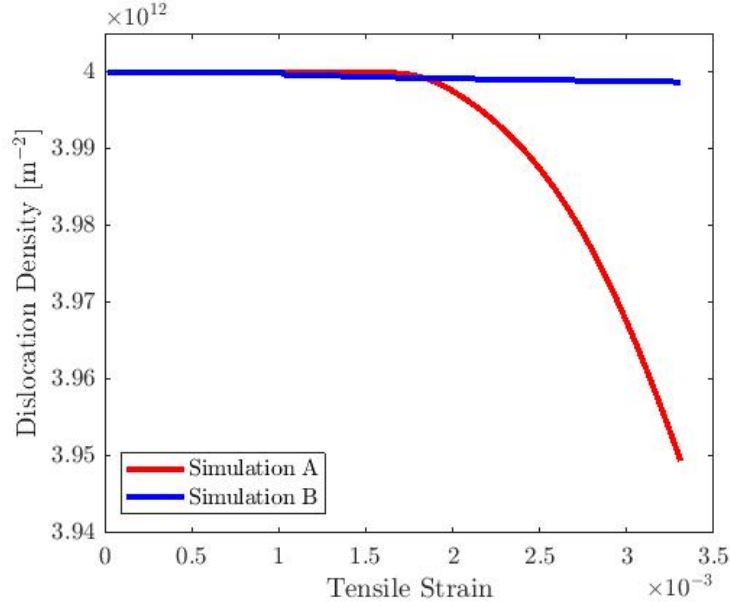
Figure 19. Dislocation density evolution within cells for Simulation A and B.

3.5.2   *Mesoscale Validation Using Digital Image Correlation*

Individual terms for dislocation density evolution are often numerically quantified using discrete dislocation dynamics simulations [25], and while these high order models are useful in describing the implications of different hardening modes, their predictions must be validated against experimental data. It has been considered that these terms can be determined experimentally by studying the results, at different deformation stages, of several latent hardening tests designed to induce different forest densities on slip systems [70]. In theory, one can use transmission electron microscopy (TEM) to examine the resultant dislocation content from each experiment, and determine the individual effects of each term on overall dislocation evolution. However, the difficulty in measuring dislocation densities with this approach leads to large uncertainties in any experimentally determined coefficients. As a result, individual quantities for dislocation generation and annihilation are, at best, considered rough estimates, and are often found by simply

64

guessing their values after a determination of their ratio from the slope of hardening in the bulk response. The following approach described below considers using a more accessible method of characterization; strain fields measured from DIC to calibrate these terms and reduce the overall parameter space.

From the discussion in Chapter 2, DIC will provide strain maps with levels of uncertainty which are in part dictated in part by pattern quality and subset window selection. Therefore, in order to use experimental in-plane strain maps to limit the parameter space, the strain fields outputted from simulations must differ locally from each other by magnitudes greater than the DIC uncertainty determined in Chapter 2. This means that, at a given coordinate location, the difference in predicted strain between Simulation A and Simulation B must be greater than the deviation level of DIC measurement at that location. Otherwise, a strain map measured from DIC will be considered too erroneous to discern between simulations at that coordinate.

The axial strain field from Simulation A, and its absolute difference as compared to axial strains from Simulation B, are shown in Figure 20(a) and Figure 20(b) respectively. Each simulated strain field is produced from respective simulations at matching locations of applied strain, approximately 0.34%. It can be seen that there are in fact some considerable differences between the two strain fields, especially at the locations near the grain boundary junctions where strains are largest. At initial glance, these differences look to be well within the levels of uncertainty discussed in Chapter 2. As shown in Figure 20(b), the maximum absolute difference between local strains from either simulation is 1.1×10^{-3}, and is found at coordinate locations near grain boundaries, where strain magnitude is furthest from the mean 0.34% applied.
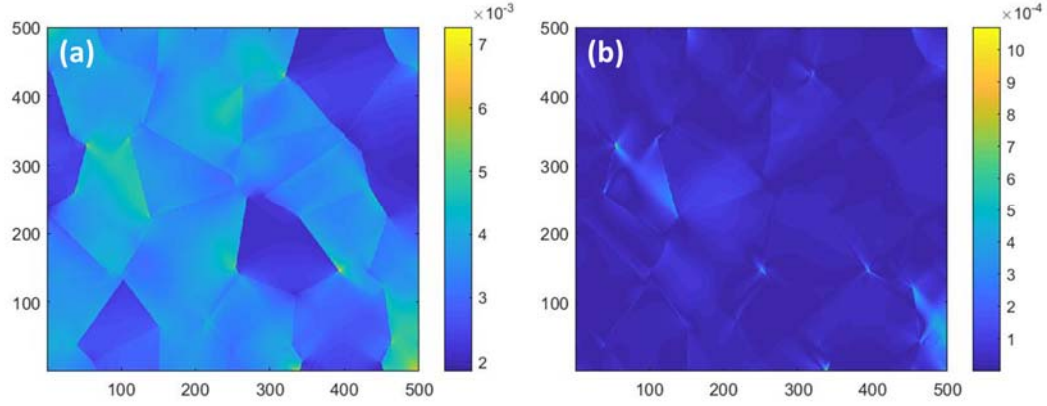
Figure 20. (a) Axial strain field from Simulation A at 0.034 applied strain. (b) Local difference between Simulation A and B axial strain fields at 0.034 applied strain.

In a more quantitative analysis, Figure 21 compares the local absolute difference between simulation strain fields with the expected deviation in DIC measured strain using Equation 17 from Chapter 2. Similar to Figure 9 in Chapter 2, the absolute difference between strain is calculated at every voxel, and the data is discretized into 10 evenly-spaced bins based on the local strains from Simulation A. The median of each bin is plotted using black dots with connecting lines and the shaded region represents the spread of data within one standard deviation from the median value. The DIC resolution, Equation 17, is plotted as a function of the material response in Simulation A, using pattern P4 and the largest subset size (~50 um), which in combination produce the lowest deviation levels for this strain range. Plotting according to strains experienced Simulation A assumes it is the correct simulation, but nearly identical results are achieved when plotting according to Simulation B strains.

It can be seen that the differences between simulated strains are almost always less than the expected deviation in DIC measurements. Only between applied strains 4.5×10^{-3} and 6.5×10^{-3} does the in-plane strain map uncertainty dip slightly within

one standard deviation of simulated strain map differences. This implies that DIC-measured strain data could perhaps discern these parameter sets in a limited strain range across a handful of voxels.
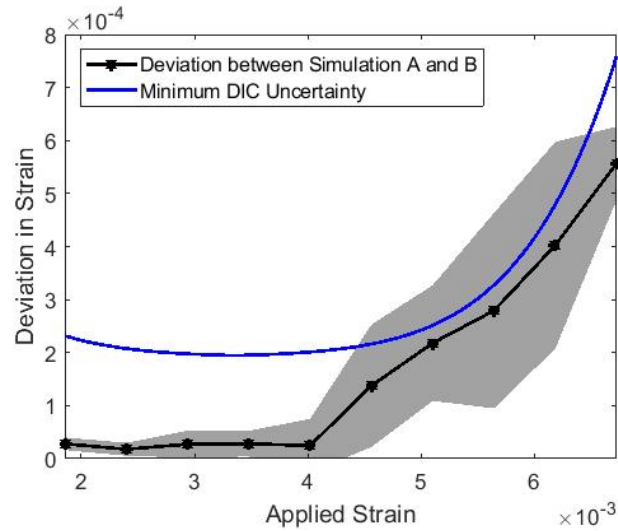
Figure 21. Comparison of DIC uncertainty and local differences in axial strain from Simulations A and B.
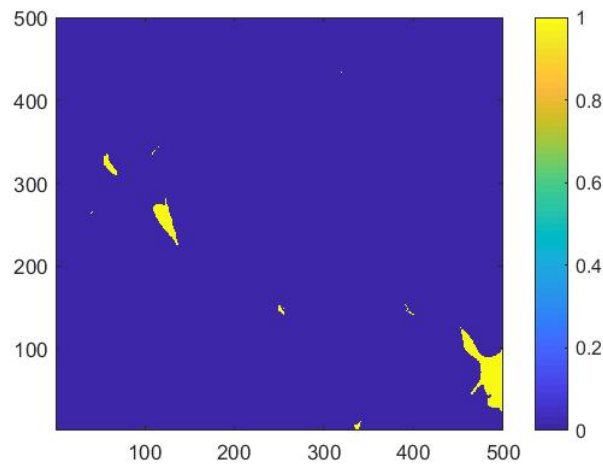
Figure 22. Areas of sample where local DIC uncertainty is less than local differences between Simulation A and B

A two dimensional visualization of this DIC ability is plotted in Figure 22. This data is generated by calculating the expected DIC deviation at every voxel according to strains from Simulation A and Equation 17, then locally comparing this expected deviation to the difference between Simulations A and B, Figure 20(b). In Figure 22, areas shaded blue are where the local differences between each simulation are less than expected DIC deviation. In these regions, it is assumed that uncertainty levels in DIC measurements are too large to discern simulations. Areas shaded yellow are those where simulated strains differ by a magnitude greater than DIC deviation. These yellow areas imply where in-plane strain mapping could in fact be used to differentiate simulations, and therefore rule out the parameter combination used to generate Simulation B.

As shown, in Figure 22 only ~1% on the map from Simulation B can be ruled out using in-plane strain maps measured from DIC, when assuming that Simulation A is correct. (Once again, accomplishing the same analysis but taking Simulation B as true yields similar results). Further, it must be noted that the analysis used to determine error in DIC strain fields from Chapter 2 neglects several physical sources of uncertainty (lens aberration, lighting gradients, etc.). These errors will certainly exist in any real application of DIC, and in the previous chapter these were shown to increase deviation in measurement by at least a factor of 3, which would not have permitted parameter set reduction in the current example. Regardless, it is shown here that by adjusting dislocation evolution terms, k_1 and k_2, the local material response will vary while still maintaining the same bulk output. This variance in local material response is in fact captured by in plane strain fields, and therefore DIC presents a promising tool for elucidating the differences between parameter descriptions. In strain fields not shown

68

here, it was concluded that these local differences are less exaggerated when descriptions are more similar in magnitude, as one would expect. As such, the current DIC protocol practiced here would only be able to reduce a parameter space for more extreme variations in parameter descriptions, like the ones used here.

Even with the limitations in mind, it is expected that a comparison between simulations at a later stage of deformation would amplify the local differences in material response while maintaining indistinguishable bulk responses. Beyond the elastic-plastic region studied here, and perhaps even towards later stages of damage softening, it is postulated that localized plasticity differences will be more apparent among simulations, allowing more prevalent discernibility using strain fields from DIC.

In conclusion, the strategy of using a high-order model in a full-field framework, in conjunction with relatively simple mesoscale mapping techniques, such as DIC, presents a great opportunity for rapid and unique parameterization of numerical modelling. More generally, the close synthesis of experiment and modelling accomplished here will drive a process where each respective domain iteratively informs the other where improvements in current materials science understanding are necessary. As such, the scientific approach to material modelling can be continuously optimized.

CHAPTER 4.   MICROSTRUCTURALLY SENSITIVE CREEP DAMAGE LAW FOR POLYCRYSTALLINE MATERIAL SYSTEMS

4.1   Abstract

In this chapter, a microstructure-sensitive creep damage law for polycrystalline materials is added to the constitutive law by Wen et al. [26], which was described in Chapter 3. The law considers the three traditional porosity evolution regimes: void nucleation, void growth, and void coalescence which leads to fracture. Using the Gurson-Tvergaard-Needleman (GTN) model, the effect of porosity on damage is calculated, which is applied back to the material using a proper damage term. The model is employed in the same finite element framework as in Chapter 3, and as such the porosity evolution and resultant damage is calculated locally, allowing for heterogeneous damage descriptions and a full-field material response examination. Additionally, a novel method for tracking discrete void populations within a material point is presented. The damage model is described in detail in the proceeding text, and validation against high-temperature creep experiments for Grade 91 Fe-9Cr-1Mo steel is presented.

4.2   Damage Law Description and Background

The porosity of a material governs the damage softening response, and as such the fidelity of any damage model will rely heavily on the accuracy of void evolution descriptions. On the continuum level, porosity has been investigated in some detail for general plastically deforming materials. But it has been shown that in the case of

70

polycrystalline material systems, localization of plastic flow and porosity occurs at microstructurally important features, namely grain boundaries and precipitates [71]. Further, different mechanisms for cavitation and growth exist, beyond simple plastic dilatation, (e.g. diffusional vacancy transport, viscoplastic dislocation flow, etc.) and depend on the thermomechanical loading conditions that the material is subject to. Regardless, it has been ubiquitously accepted that voids evolve through a three-stage process: nucleation, growth, and finally coalescence. Each regime is described in this section, within the context of a creeping polycrystalline structure, and a microstructurally sensitive damage model formulated is proposed.

However, before discussing the origin of these void evolution terms, it is useful to describe the method by which porosity at each material point is calculated. In this model, a novel strategy for maintaining discrete populations of voids within a material point is implemented, so that newly initiated voids can appropriately evolve independently of previously initiated voids. A tabular dataset is used to store the void population number density, $\tilde{n}_i$, created at each time step, or iteration i, and that population's collective void radius, a_i, which is updated in each subsequent time step. The number density of a previously added void population is not modified in later time steps, but rather newly initiated voids are added to the end of the table in a new row, and tracked throughout the rest of the simulation. A porosity term for a given material point can be calculated by simply summing each void population's product of number density and updated volume, as follows:

$$f_{ti} = \frac{4}{3}\pi h(\psi) \sum_{i}^{ti} \tilde{n}_i a_i^3 \qquad (69)$$

where ti is the total number of time steps (or current iteration number) and $h(\psi)$ is a geometry factor for relating void radius to volume from [72] which is described later on. Mean spacing, $\bar{b}_{ti}$, at a material point can approximated based on porosity using the following:

$$\bar{b}_{ti} = \left(\frac{3}{4\pi f_{ti}}\right)^{1/3} \qquad (70)$$

4.2.1 Void Nucleation

Void nucleation is the result of an aggregation of vacancies due to a stress- and temperature-dependent diffusion process. This process can be initiated at second-phase particles, which have either cracked or debonded from the surrounding material matrix due to a surpassed interfacial stress. Additionally, void initiation can arise from grain boundary sliding, when the diffusional or plastic flow can no longer accommodate the movement of neighboring grains with respect to each other. In the case of precipitate-initiated void nucleation, the process is theoretically stress-dependent, but is often modeled using a strain-based criterion for particle cracking and void inception. In studies from Gurland [73] it was determined that, in addition to effects of particle size and orientation with respect to loading, cracking of particles could be represented by a linear relationship with total applied strain. However, Argon [74] later determined that the cracking or decohesion of rigid particles favors a criterion based on surpassing a critical

stress normal to the matrix-particle interface. In both cases, it was noted that when particles are larger in size and/or orientated normal to the maximum tensile loading direction, they will break in at an earlier stage of loading.

Chu and Needleman [75] acknowledged both criteria and postulated that in either case the magnitude necessary to initiate voids must have some statistical variance, which can be modeled using a simple normal distribution centered about the mean critical nucleation term. This approach conveniently accounts for an inherent distribution of particle sizes, shapes, and orientations present within the material system, in a phenomenological manner. In a later work by Needleman and Tvergaard [76], the stress- and strain-based nucleation conditions proposed in [75] were studied for varying precipitate sizes. In their work, it was determined that the cracking of large particles could be captured most accurately using a critical stress criterion, while smaller particles favored a critical strain criterion.

With these previous investigations in mind, a void nucleation rule is proposed here which considers both the stress-based and strain-based nucleation conditions in combination. Variance of each nucleation criterion is incorporated in the same manner as [75], and each process is weighted to prescribe an effective percentage of stress- and strain-based nucleation to total void number density, $\tilde{n}_{ti}$, at the current time-step, ti

$$\tilde{n}_{ti} = \tilde{n}_{sat}[R_\varepsilon F(\varepsilon_d) + (1 - R_\varepsilon)K(\bar{\sigma}, \sigma_{kk})] \tag{71}$$

In the above, $\tilde{n}_{sat}$ is the saturation number density of voids, F is the number density of voids nucleated as a function of strain, ε_d, which has been adjusted for the porosity, K is

the number density of voids nucleated as a function of the updated flow stress, $\bar{\sigma}$, and hydrostatic stress, σ_{kk}, and R_ε is the proportion of strain-based nucleation on total number density of voids. The strain- and stress-based nucleation criteria are given as follows:

$$F(\varepsilon_d) = \frac{1}{2}\left[1 + \mathrm{erf}\left(\frac{\varepsilon_d - \varepsilon_c}{\sqrt{2}V_\varepsilon}\right)\right], \tag{72}$$

$$K(\bar{\sigma}, \sigma_{kk}) = \frac{1}{2}\left[1 + \mathrm{erf}\left(\frac{\bar{\sigma} + \frac{1}{3}\sigma_{kk} - \sigma_c}{\sqrt{2}V_\sigma\sigma_y}\right)\right], \tag{73}$$

where ε_c and σ_c are the mean critical nucleation strain and stress respectively, and V_ε and V_σ govern the variance in nucleation strain and stress.

The decision to combine both stress and strain criteria was made to capture particle cracking behaviors which are best predicted by each respective process Figure 23 shows an example of the number density of voids nucleated by either process with strain-dependent voids plotted in Figure 23(a) and stress-dependent voids plotted in Figure 23(b).

These two processes are independent of each other, and can be used to simultaneously describe two separate populations of particle: one which cracks from a surpassed critical strain and one which cracks from a surpassed critical stress. Considering the work of Needleman and Tvergaard [76] discussed earlier, this might be used to imply a bimodal particle size distribution, but could also describe distributions in shape, particle type, and orientation with respect to loading. Further, the variance in both

74

Equations 72 and 73 allow for smooth transition between particle populations when appropriate.
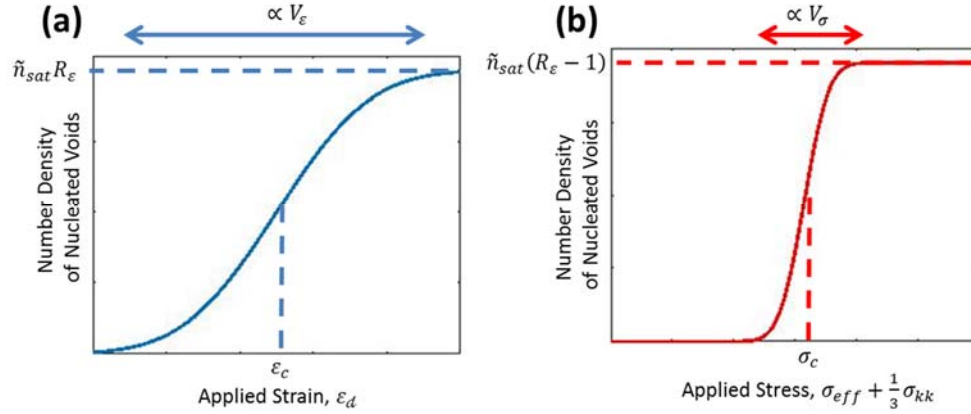
Figure 23. Example depictions of void nucleation due to (a) strain per Equation 72 and (b) stress using Equation 73.

The decision is made to limit void nucleation to those voxels which lie along the grain boundaries. This simplification will certainly neglect potential damage evolution within grains, but is in line with experimental and theoretical observations that conclude porosity evolution is highly preferential to grain boundaries [71].

4.2.2 *Void Growth*

To account for creep cavity growth, two main mechanisms are considered in the present work: void growth due to viscoplasticity and the flow of dislocations (or creep growth), and void growth due to a net flux of vacancies towards a cavity via diffusion (or diffusion growth). Given the temperature and stress-state which will be considered in the present work, it is inferred from Ashby's deformation map [30] that these two mechanisms of creep will be active and therefore must be accounted for in overall void growth calculation.

Creep void growth was initially studied by McClintock [77, 78] and Rice and Tracey [79], then later extended to the modern formula proposed by Budiansky et al. [80]. McClintock [77, 78] considered a single long cylindrical cavity in a non-hardening material, subject to remote loading in various axes. In [77], it was determined that relative void expansion is exponentially dependent on the magnitude of stress transverse to the cylinder axis. Rice and Tracey [79] studied the case a spherical void in a non-hardening material, and concluded that hydrostatic stresses are responsible for void growth and can be considered large enough to overcome shear components so that voids will maintain quasi-spherical shape. Budiansky [80] studied both cylindrical and spherical cases and extended each void growth model to properly account for large stress triaxialities and different hardening behaviors. The resulting formula for void growth from Budiansky's [80] investigation was a power-law dependence on stress triaxiality for void growth.

Diffusional void growth was first examined by Hull and Rimmer [81], later corrected by Weertman [55], in which a periodic array of spherical voids along a grain boundary was modeled to grow by an atom transport process through void surfaces. In their descriptions it was assumed that vacancy diffusion within grains is rapid enough, when compared to diffusion along grain boundaries, so that voids will grow quickly and maintain quasi-spherical shape. Later on, Chuang et al. [82] reconsidered the case of spherical void growth, and also one of slower, crack-like void growth due to rapid diffusion and void extension along grain boundaries. Both cases examined in Chuang et al. [82] resulted in a description of void growth dependent on temperature and the stress component resolved in the direction normal to the grain boundary.

Both the work of Budiansky [80] and Chuang et al. [82] were revisited and combined by Needleman and Rice [72], with slight improvement from Chen and Argon [83]. In [72] it was noted that in conditions of creep loading, both viscoplastic dislocation flow and diffusional vacancy transport mechanisms are active, which leads to void growth rates much greater than if each mechanism was considered independently. The coupling of the two mechanisms was shown to reduce the diffusive path length along grain boundaries, facilitating matter transport through cavity surfaces, therefore accelerating void growth in a quasi-spherical manner.

The final model chosen to describe void growth is the one developed by Needleman and Tvergaard [72], adjusted by Chen and Argon [83]. Rewritten slightly for the current framework, the change in radius, $\dot{a}_i$, for each void population i, is the sum of void growth due to diffusion, $\dot{a}_i^d$, and the flow of dislocations, $\dot{a}_i^c$, which are all functions of the current void population radius, a_i:

$$\dot{a}_i(a_i) = \dot{a}_i^d(a_i) + \dot{a}_i^c(a_i) \tag{74}$$

$$\dot{a}_i^d(a_i) = \frac{\mathcal{D}}{a_i^2 h(\psi)} \frac{\sigma_n - (1 - f_{adj})\sigma_s}{\ln\left(\frac{1}{f_{adj}}\right) - \frac{1}{2}(3 - f_{adj})(1 - f_{adj})} \tag{75}$$

$$\dot{a}_i^c(a_i) = \begin{cases} \frac{1}{2}\dot{\varepsilon}_{eq}^p a_i \left[\alpha_n \left|\frac{\sigma_{kk}}{3\sigma_{eq}}\right| + \beta_n\right]^n, & \text{for } \left|\frac{\sigma_{kk}}{3\sigma_{eq}}\right| > 1 \\ \frac{1}{2}\dot{\varepsilon}_{eq}^p a_i [\alpha_n + \beta_n]^n \frac{\sigma_{kk}}{3\sigma_{eq}}, & \text{for } \left|\frac{\sigma_{kk}}{3\sigma_{eq}}\right| < 1 \end{cases} \tag{76}$$

In the above equations $\mathcal{D}$ is a diffusivity term for the grain boundary, σ_n is the local stress in the direction normal to the grain boundary, f_{adj} is an adjusted porosity term, σ_s is the

sintering stress, ψ is the angle of the void with respect to the grain boundary, h is a function which adjusts the void volume based on ψ, and α_n and β_n are constants based on the hardening exponent, n. In the above, α_n and β_n are as follows:

$$\alpha_n = \frac{3}{2n} \tag{77}$$

$$\beta_n = \frac{(n-1)(n+0.4319)}{n^2} \tag{78}$$

which Budiansky originally derived in his void growth analysis [80]. The void geometry function $h(\psi)$ is given by:

$$h(\psi) = \frac{(1 + \cos\psi)^{-1} - \frac{1}{2}\cos\psi}{\sin\psi} \tag{79}$$

where typical value for ψ is ~70 degrees and therefore $h(\psi) = 0.61$ [82].

The sintering stress gives an effective surface tension of the voids, determined by the free surface energy of the void, γ_s, and the void's geometry:

$$\sigma_s = \frac{2\gamma_s \sin\psi}{a_i} \tag{80}$$

Sintering will occur when the surface tension of the void exceeds the normal stress applied to the void, i.e. where the numerator of Equation 75 is equal to zero. At initial phases of void evolution, when porosity is very low, this implies a critical void radius:

$$a_c = \frac{2\gamma_s \sin \psi}{\sigma_n} \tag{81}$$

above which voids will grow, and below which voids will close-up by diffusion. This critical size, which varies based on local stress, is assigned to nucleated void populations that are added to the end of the discrete population table described above.

In Equation 75 Needleman and Rice [72] take the grain boundary diffusivity term as the following:

$$\mathcal{D} = \frac{D_{B0}\delta_B\Omega}{kT} \exp\left(-\frac{E_a^v}{kT}\right) \tag{82}$$

where D_{B0} is the grain boundary diffusion constant, δ_B is the thickness of diffusion layer (i.e. the width of high diffusivity centered around the grain boundary), and E_a^v is the activation energy for a vacancy. Mendelev and Mishin [56] consider the activation energy as the sum of vacancy formation and migration energies, as follows:

$$E_a^v = E_f^v + E_m^v \tag{83}$$

The adjusted porosity term for each void population is important for determining the balance of diffusion and creep controlled cavity growth, and is given below:

$$f_{adj} = \max\left\{\left(\frac{a_i}{\bar{b}_{ti}}\right)^2, \left(\frac{a_i}{a_i + 1.5L}\right)^2\right\} \tag{84}$$

where L is a material length scale term based on the diffusivity, remote equivalent stress, and equivalent creep rate:

$$L = \left(\mathcal{D} \sigma_{eq} / \dot{\varepsilon}_{eq}^{p} \right)^{\frac{1}{3}} \tag{85}$$

Needleman and Rice [72] propose this L term to determine the balance of viscoplastic void growth and diffusion void growth. In physical terms, it is considered the grain boundary length along which diffusion occurs towards a void, which has been shorted by the presence of creep void growth. When a/L is small ($a/L < 0.1$), voids grow almost entirely in the diffusion/viscoplastic regime (governed by Equation 75), and their volumetric growth rates are very high. When a/L is large ($a/L > 10$), voids are thought to grow exclusively by creep (governed by Equation 76), matching the formula given by Budiansky [80] for high stress triaxialities. Between these values of a/L, the contribution of both void growth mechanisms is significant and each process must be taken into account.

4.2.3   Void Coalescence

The final stage of void evolution, coalescence, is the least studied regime of porosity in plastically deforming materials. This stage is described as the point when voids have grown sufficiently with respect to their spacing, and begin to combine and form micro-cracks which eventually lead to macro-cracking and bulk material failure. Given the preference of voids to nucleate and grow at grain boundaries during primary and secondary stages of creep, it has been assumed that void coalescence leads to

intergranular cracking and bulk failure which is strongly dependent on the polycrystalline layout.

The proposed criteria for entering this regime of porosity varies from theoretical physical descriptions of void interactions, to simple critical porosity threshold approaches above which an empirical factor simple scales overall porosity. Physical-based descriptions imply that intervoid ligaments will fail upon reaching geometry where their material plastic load limit experienced. Others have simply considered that once void radius equals void spacing, voids coalesce and material failure is initiated. Both claims are intuitively valid, but have not been investigated in great detail, either theoretically or experimentally, especially for the case of creeping polycrystalline materials. Therefore the simple empirical criterion suggested by Tvergaard and Needleman [84] in their modification of Gurson's damage model is used:

$$
f^* = \begin{cases} f_{ti} & \text{if } f \leq f_c \\ f_c + \kappa(f_{ti} - f_c) & \text{if } f > f_c \end{cases}
\tag{86}
$$

where f_c is the critical porosity above which coalescence begins, and κ is a coalescence effect factor which scales porosity magnitudes that are above the critical threshold. This coalescence factor is given by

$$
\kappa = \frac{1/q_1 - f_c}{f_f - f_c}
\tag{87}
$$

where f_f is the porosity of the material at failure. This porosity adjustment is based on the experiments from Goods and Brown [85], where it was determined that coalescence

begins when porosity reaches approximately 0.15, and Anderson [86] found that that failure occurs when the volume fraction of voids is equivalent to $f_f = 0.25$.

4.2.4 Local Damage Description

The incorporation of damage and fracture in ductile materials is often based on the Gurson-Tvergaard-Needleman (GTN) damage model. In the original work [87] Gurson studied the case of a single void in a rigid-plastic, incompressible unit cell, and proposed that the evolution of the yield surface can be described based on the stress state and the ratio of void size to unit cell size, i.e. porosity. Tvergaard and Needleman later modified the model slightly to better fit experimental data for tensile testing of round bars with periodic arrays of spherical or cylindrical voids [84]. The final GTN model describes the yield function as the following:

$$\Phi = \left(\frac{\sigma_{eq}}{\bar{\sigma}}\right)^2 + 2q_1 f^* \cosh\left(q_2 \frac{\sigma_{kk}}{2\bar{\sigma}}\right) - 1 - (q_1 f^*)^2 \tag{88}$$

where Φ is considered the plastic potential, σ_{eq} is the equivalent stress, $\bar{\sigma}$ is the effective stress, or updated yield stress, σ_{kk} is the trace of the stress tensor, f is the porosity, and q_1, and q_2 are constants.

In Equation 88, the updated yield stress is implicitly solved for when $\phi = 0$. This new yield stress gives some idea of the damage which the material has accumulated, and in this text a damage term, d, is defined to give a proper measure of the damage based on the ratio of new and original yield surfaces:

$$d = \frac{\bar{\sigma}}{\sigma_{eq}} \qquad (89)$$

To adjust the constitutive law of Wen et al. described in Chapter 3, local damage is applied to the mean resolved shear stress at the material point:

$$\bar{\tau}_d^s = d\bar{\tau}^s \qquad (90)$$

where $\bar{\tau}_d^s$ is the resolved shear stress, adjusted for damage. This simulates an increase in applied load on each slip system locally, which in turn leads to an increased slip rate i.e. plastic flow localization. In his derivations Gurson included an important assumption, which was that only material volume should transfer loads (i.e. cavities cannot support loads). With this in mind, the resultant strain rate at each material point is adjusted based on the porosity:

$$\dot{\varepsilon}_d^p = (1 - f^*)\dot{\varepsilon}^p \qquad (91)$$

where $\dot{\varepsilon}_d^p$ is the adjusted plastic strain rate at a material point.

The iterative solve of the numerical simulation from Figure 17, including the new damage law which is in red, can be visualized in Figure 24.
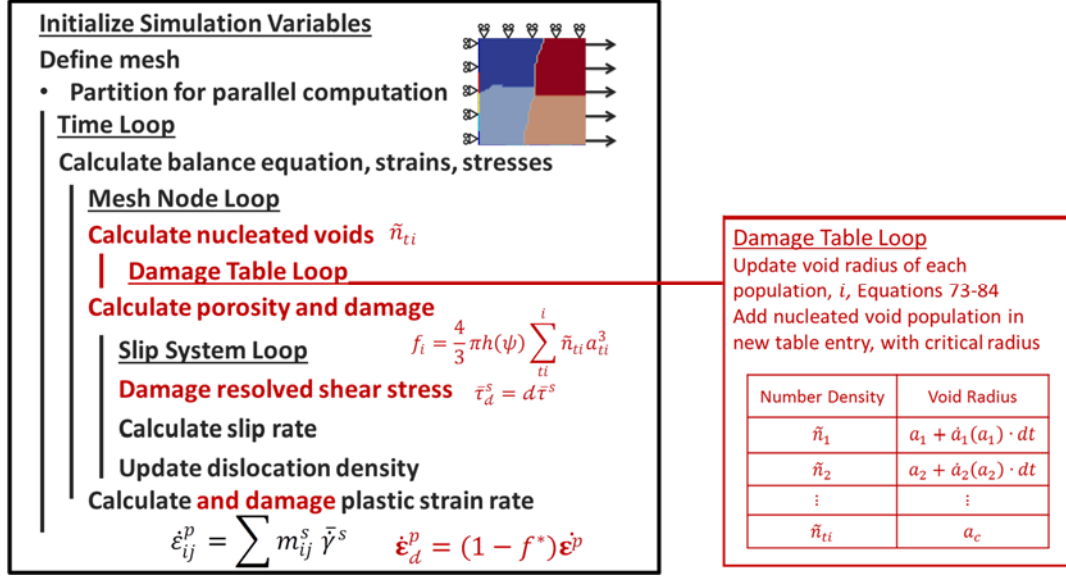
Figure 24. Iterative solve description of numerical model, included new damage law steps in red.

4.3   Results and Discussion

The material system studied in this chapter is the same Grade 91 Fe-9Cr-1Mo alloy considered in Chapter 3. Therefore, the parameters listed in Table 3 will be used to describe the same constitutive law that was presented in Chapter 3. Additional parameters are added to the model to incorporate the damage law proposed above, and these constants are listed in Table 5.

The model is employed in the FreeFem++ [66] finite element framework discussed in Chapter 3, with the same 5x5 polycrystalline grain structure modeling using 199x199x1 grid of tetrahedral elements with quadratic interpolation between nodes. The model is loaded according to the boundary conditions described in Equation 60, using the traction surface area integral to apply different creep loads. The creep and creep rates from simulation are calibrated against the high-temperature (973 K) creep tests from

Basirat et al. at three stresses, 80 MPa, 100 MPa, and 150 MPa [71]. The predicted creep

and creep rates from simulation are compared to these experimental results in Figure 25.

Table 5. Damage parameters for FeCrMo alloy.

| Parameter		Fe-Cr-Mo
ψ	Void geometry factor	70°
R_ε	Weight of strain-based nucleation	0.2
$\tilde{n}_{sat}$	Number density of potential nucleation sites	10^{24}
ε_c	Critical strain for void nucleation	0.6
V_ε	Variance of nucleation strain	0.168
σ_c	Critical stress for void nucleation	$0.27\sigma_y$
V_σ	Variance of nucleation stress	$1.44\sigma_y$
n	Hardening exponent	6.9
γ_s	Free surface energy of void	50 mJ/m
δ_B	Mass density	8000 Kg/m³
D_{B0}	Diffusion constant at grain boundary	$50 \times D_v^0$
f_c	Critical porosity for coalescence	0.10
f_f	Porosity at failure	0.30
q_1	GTN equation constant	1.5
q_2	GTN equation constant	1.0
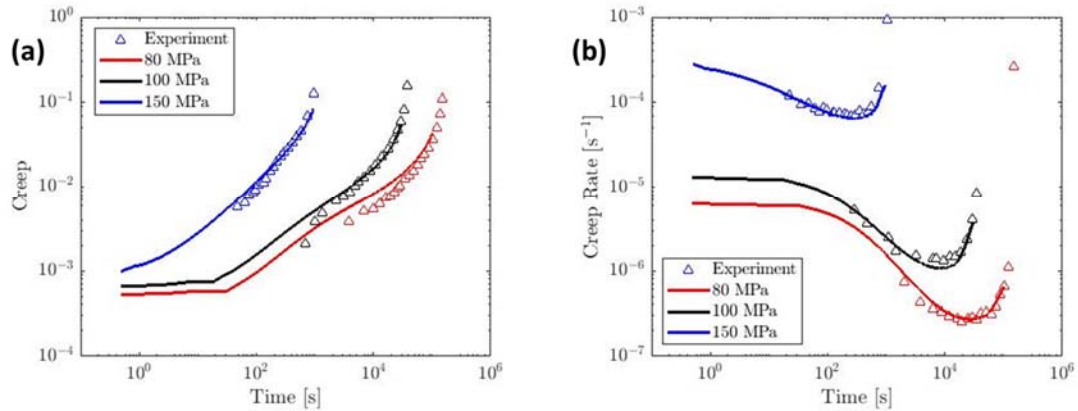
Figure 25. Creep and creep rate predictions from numerical simulation compared to experimental data from Basirat et al. [71]

From Figure 25, it can be seen that numerical results agree excellently with the

experimental creep data at each applied loading. Material response predictions are

particularly accurate in the secondary and tertiary creep regimes, where sensitivities to relatively small variations in loading are appropriately observed by the model.
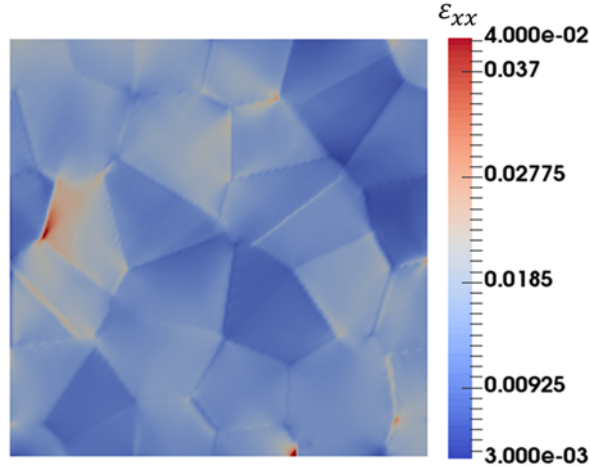

Figure 26. Axial strain field from tertiary creep regime for 80 MPa, 973 K loading.

Implementation of the model in a finite element framework allows for a full-field examination of material response. Figure 26 shows the axial strain field measured in the polycrystal, for the 80 MPa, 973 K loading condition at a location well within the tertiary creep regime (2.57×10^4 seconds or 7.13 hours). At this location of creep testing, the average strain in the material is 1.23×10^{-4}, but it can be seen that local strains vary significantly and can exceed 3 times this mean magnitude, typically near grain boundary junctions.

The local evolution of voids across the material can be investigated in a similar manner. In Figure 27 the porosity field of the polycrystal is shown at the three different stages of creep, for the 80 MPa, 97K loading condition. In Figure 27(a), local porosities predicted by the model after 2 seconds of loading indicate that within the primary regime of creep, voids have only just begun to nucleate and maximum porosity is approximately

2.1×10^{-4}. In Figure 27(b), porosity in the secondary regime of creep is illustrated, after 820 seconds (0.2 hours) of loading, and it can be seen that void growth is well underway, and local porosities exceed 2.5×10^{-3}. Figure 27(c) shows that in the final creep regime, at 2.57×10^4 seconds (7.13 hours) where voids have begun to coalesce, void size-spacing ratios have reached saturation porosity, 0.3, in many locations, and intergranular fracture has perhaps initiated at the grain boundary in the lower right corner of Figure 27(c).

Figure 27 illustrates that maximum local porosity is found at grain boundaries which are transversely-oriented to the loading direction. This is expected from the theory outlined in Equations 74-76, where particularly for diffusional void growth, a larger stress-component that is resolved normal to grain boundaries will maximize void growth. Further, experiments [71] have shown this void presence dependency on grain boundary direction. There is an exception to this rule in Figure 27(a), however, where maximum porosities in primary creep are actually found at grain boundaries which lie almost parallel to the loading direction. This is due to the minimum void criterion in Equation 81, which dictates that a smaller normal component of stress will increase the critical nucleation radius. Since this model uses void nucleation criteria which are independent of this minimum size condition, it is possible for voids to nucleate under a small normal stress and therefore initiate with a large radius. This should be considered a discrepancy with the current model and implies that more coupled approach to void nucleation and growth might be appropriate, perhaps one in which the aggregation of vacancies that form minimum void sizes for "nucleation" (and therefore continued growth) is described. Regardless, the material response from Figure 27 should ideally inform the next iteration

of experiments, so as to validate assumptions and reveal further discrepancies of the current model.
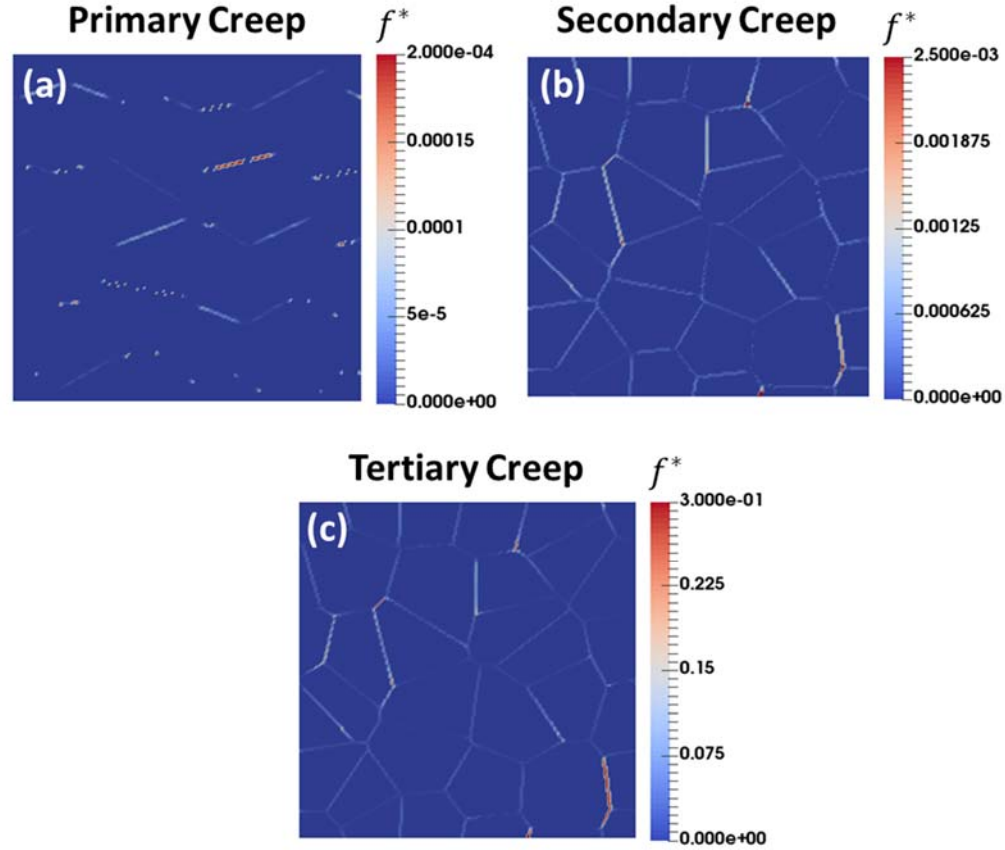
Figure 27. Local porosity in the (a) primary creep, (b) secondary, and (c) tertiary creep regimes.

Values which govern the proposed damage law are studied in Figure 28, along time normalized with time to rupture, t_r. Rupture is simply considered when the material experiences a creep rate increase of 10%. First, mean damage term and porosity across the material over time is shown in Figure 28(a) and Figure 28(b). It can be seen that damage and porosity evolution follow a trend of exponential increase over time and, respectively, are nearly identical between simulations at different applied stresses. The mean damage term at rupture is 1.072, 1.060, and 1.067 for 80 MPa, 100 MPa, and 150

MPa loading, respectively. Mean porosity at rupture time is 0.032, 0.0257, and 0.0237 for 80 MPa, 100 MPa, and 150 MPa loading, respectively. These results imply that, at a given temperature, porosity evolution and subsequent damage calculation are independent of applied stress when studied along normalized time to rupture.
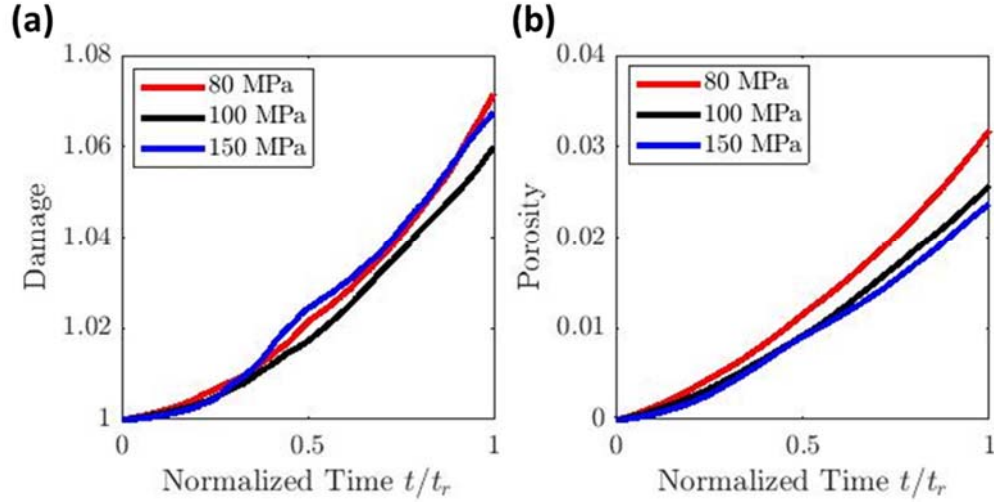
Figure 28. Mean damage and porosity across material over time to rupture.

In Figure 29(a) and Figure 29(b), respectively, the mean size and number density of voids are shown. Unlike Figure 28, these terms have been averaged only over locations where void initiation is allowed (at grain boundaries). Additionally, in Figure 29(b) void radius calculations are weighted by each respective number density of void population. From Figure 29(a), it can be seen that voids nucleate at a slightly increasing rate over time, and that void nucleation is at least an order of magnitude greater for the high stress-state (150 MPa) compared to the lower stresses. Specifically, for this 973K temperature state, the number density of voids half-way through each creep test is 2.2×10^{21}, 1.2×10^{20}, 5.5×10^{19} voids per cubic meter for tensile loading at 150 MPa, 100 MPa, and 80 MPa respectively. These magnitudes for void number density are considered reasonable

when compared to the number density of MX precipitates in the current material system, 3×10^{20} m^{-3}. Since voids often nucleate at these second-phase particles [71], one would expect total number density to slightly exceed this magnitude, given the additional, but significantly lowered, potential for void nucleation elsewhere.
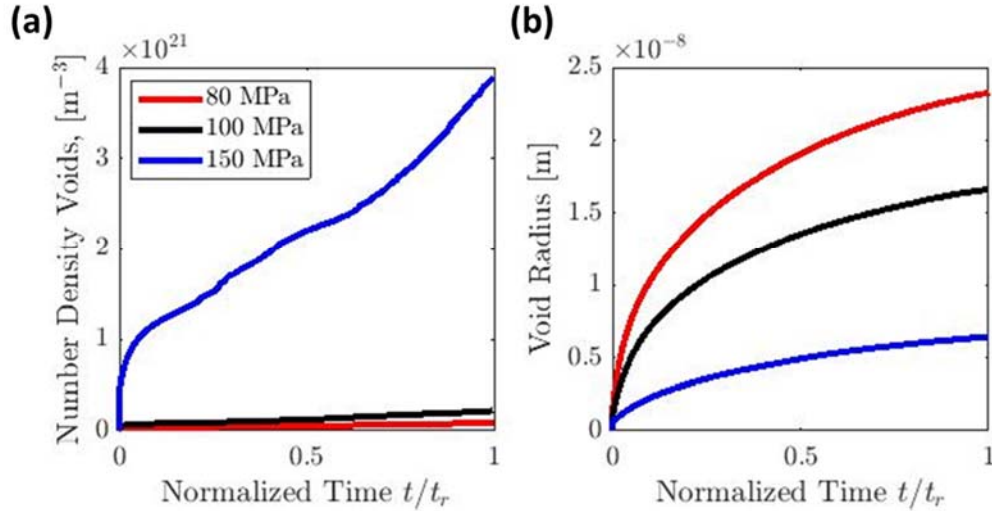
Figure 29. Mean (a) number density and (b) void radius at potential nucleation sites over time to rupture.

In Figure 29(b) it can be seen that average void size tends to increase at a decreasing rate. This is due to the continued increase in void number density shown in Figure 29(a), where small initial voids tend to make up a larger percent of the entire material point population as each creep test continues. Additionally, while it was seen that low stresses will limit the nucleation of voids, it seems that the voids which are present will grow faster on average in low stress regimes than in high stress regimes. Indeed, final mean void radius increases from 6.4, to 17, to 23 nm when decreasing stress from 150 MPa, to 100MPa, to 80 MPa. Note that in this work, the ratios of void radii to the diffusion length parameter from [72], for each simulation, are approximately $a/L =$

2×10^{-1}, which is within the regime of combined creep and diffusion growth described earlier.

The respective contribution of local strain and local stress to void nucleation is shown in Figure 30(a) and Figure 30(b), and mean value calculation is again limited to material points at grain boundaries. Figure 30(a) shows that at a given temperature, the number of voids which have nucleated due to surpassing a critical strain threshold is within the same order of magnitude for the three stress-states studied here. This is expected considering that for each stress, the axial creep magnitudes given in Figure 25(a) are similar in magnitude and only shifted by time. The number density of voids nucleated by the strain criterion is 2.7×10^{19}, 2.8×10^{19}, and 3.7×10^{19} voids per cubic meter for 80 MPa, 100 MPa, and 150 MPa loading respectively at the midpoint of each creep test. On the other hand, Figure 30(b) shows that higher applied stresses will intuitively initiate more voids when using the stress-based criterion. At the midpoint of each creep test, the number density of voids nucleated by stress is 2.9×10^{19}, 9.6×10^{19}, and 2.2×10^{21} voids per cubic meter for 80 MPa, 100 MPa, and 150 MPa loading respectively. For both results presented in Figure 30(a) and Figure 30(b), the effect of selecting a mean critical value and including some statistical variance is clearly shown. While Figure 23 is for a generic selection of variables, and is plotted along different x-axes than Figure 30(a) and Figure 30(b), it can be used to show that in these creep tests, on average, voids have only nucleated according to the lower half of each respective cumulative distribution. Without including this variance, void number density would have been significantly limited, and while a reduced mean nucleation criteria could have

been used to maintain bulk response accuracy, it would have been based on a sort of "all-or-nothing" approach to void nucleation.
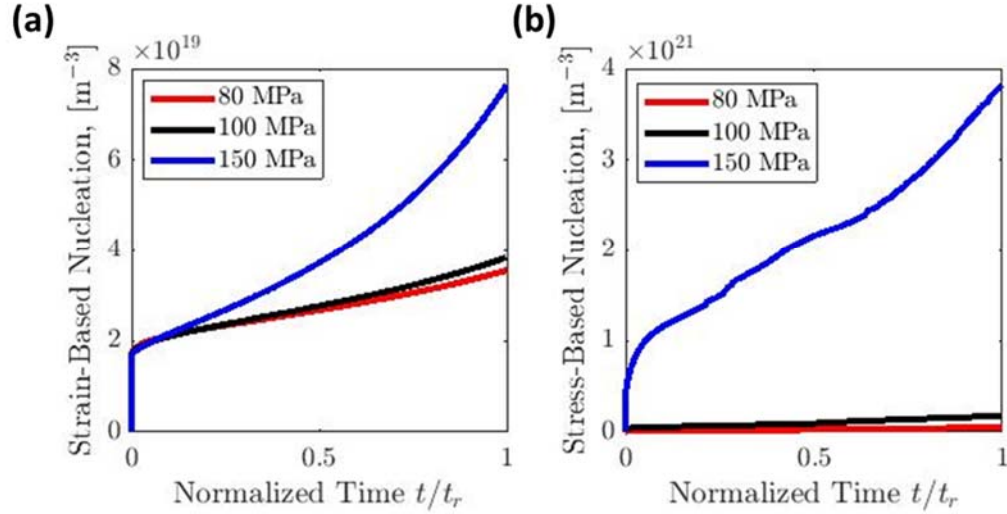
Figure 30. Mean values for (a) strain-based nucleation and (b) stress-based nucleation.

Predictions of bulk material response are most accurate for the current model when percent of nucleation due to strain is 20%, implying that perhaps 20% of all second phase particles, in this FeCrMo material system, crack according to a critical strain criterion. This could be used to imply that this percent population of particles is below a critical size, and/or are shaped or oriented in a particular manner that prohibits stress-based nucleation modeling. In any case, such statistical differences are phenomenologically captured in the current work using both nucleation criteria, without an explicit description of particle geometry effects.

Figure 31. Mean growth rate due to (a) diffusional vacancy transport and (b) viscoplastic creep flow of dislocations at potential nucleation sites over time to rupture.

Mean void growth rates due to diffusion and creep are examined in Figure 31(a) and Figure 31(b) respectively. First it can be seen that gr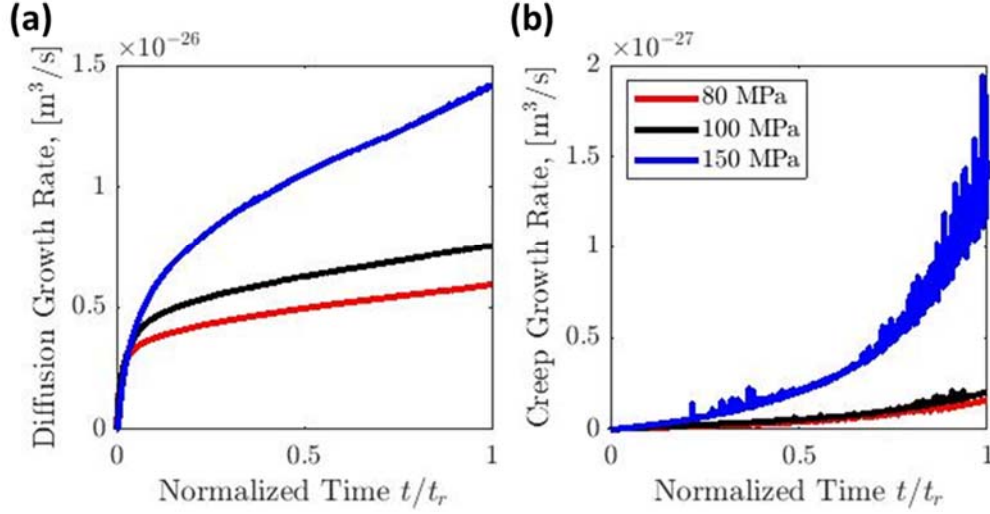owth rates will increase with larger applied stresses, especially for growth due to the viscoplastic creep flow of dislocations. In Figure 31(a), the rate of diffusion-controlled void growth rapidly increases in the first stage of creep, and eventually reaches a linear rate as the creep simulation continues. At the midpoint of each test, the diffusional growth rate for each applied load is 5.0×10^{-27}, 6.3×10^{-27}, and 1×10^{-26} m³/s for 80 MPa, 100MPa, and 150 MPa respectively. Creep-controlled void growth shown in Figure 31(b) reveals a similar dependence on stress, but with rates which exponentially increase throughout the creep test. At the midpoint of each test, the growth rates due to dislocation flow are 4.1×10^{-29}, 5.5×10^{-29}, and 2.0×10^{-28} m³/s for 80 MPa, 100 MPa, and 150 MPa respectively. In each test, it can be seen that creep-controlled cavity growth rates tend to randomly flutter around an exponentially increasing mean value. This is attributed to the

93

dependence of creep growth rate on plastic strain rate, which itself flutters slightly based on the evolution of dislocation density in the material.

Void growth rate results from Figure 31(a) and Figure 31(b) seem contradictory to void sizes given in Figure 29(b); the stress dependency between void growth and size is opposite. This is considered to be a result of the dependency of critical void size on applied stress, discussed earlier, where smaller stresses give larger initial void radii. While this is an important note of the model limitations, it does not appear to present void radii which are of unreasonable magnitude. In the current model, voids grow between the in the nanometer and micrometer range, which is similar to void examination of damaged Grade 91 Fe-9Cr-1Mo in [71, 88].

4.4 Summary and Conclusions

In this chapter, a new microstructurally-sensitive damage evolution law was proposed and employed within a finite-element framework. Model validation against experimental data was accomplished on the bulk scale for high temperature creep testing of a Grade 91 Fe-9Cr-1Mo alloy, at three magnitudes of applied stress. Excellent agreement between experimental data, and numerical predictions was shown for both creep and creep rate. Further, implementation of the model in a finite-element framework allowed for examination of a full-field material response, giving insight into local porosity evolution as well as strain localization.

Terms which describe the damage law were examined and seen to be within physically-reasonable magnitudes, reaffirming that individual components of the law are based on sound, physical understandings of porosity evolution. However, the model

stands to be improved by using a more coupled description of void nucleation and growth, and could be further calibrated against experimental data at different temperatures and applied stresses.

Regardless, the damage law and modeling framework allow one to revisit the present understanding of creep damage in a polycrystalline material system. By accomplishing a wide range of numerical simulations, including multiaxial loading, bending, and other tests which replicate physical application, an improved understanding of material lifetime and failure modes can be obtained. One-dimensional predictions for material lifetime, from parameters such as Larson-Miller and Monkman-Grant, can potentially be redefined for improved accuracy according to further numerical results. Obviously gathering this data from simulation is favorable compared to expensive and time-consuming creep experimentation, so long as the model has a reasonable basis in physical processes occurring on lower length scales. The current model, therefore, presents potential for high-fidelity predictions of material response across a wide range of creep applications.

REFERENCES

1. Holdren, J.P., *Materials Genome Initiative White Paper*, N.S.a.T. Council, Editor. 2011. p. 18.

2. White, A., *The Materials Genome Initiative: One year on.* MRS Bulletin, 2012. **37**(8): p. 715-716.

3. Horstemeyer, M.F., *Integrated Computational Materials Engineering (ICME) for metals: using multiscale modeling to invigorate engineering design with science.* 2012: John Wiley & Sons.

4. Panchal, J.H., S.R. Kalidindi, and D.L. McDowell, *Key computational modeling issues in Integrated Computational Materials Engineering.* Computer-Aided Design, 2013. **45**(1): p. 4-25.

5. Lookman, T., F.J. Alexander, and A.R. Bishop, *Perspective: Codesign for materials science: An optimal learning approach.* APL Materials, 2016. **4**(5): p. 053501.

6. Agnew, S.R., D.W. Brown, and C.N. Tomé, *Validating a polycrystal model for the elastoplastic response of magnesium alloy AZ31 using in situ neutron diffraction.* Acta Materialia, 2006. **54**(18): p. 4841-4852.

7. Wang, H., et al., *Stress and strain relaxation in magnesium AZ31 rolled plate: In-situ neutron measurement and elastic viscoplastic polycrystal modeling.* International Journal of Plasticity, 2016. **79**: p. 275-292.

8. Berfield, T., et al., *Micro-and nanoscale deformation measurement of surface and internal planes via digital image correlation.* Experimental Mechanics, 2007. **47**(1): p. 51-62.

9. Kammers, A. and S. Daly, *Small-scale patterning methods for digital image correlation under scanning electron microscopy.* Measurement Science and Technology, 2011. **22**(12): p. 125501.

10. Kammers, A.D. and S. Daly, *Self-assembled nanoparticle surface patterning for improved digital image correlation in a scanning electron microscope.* Experimental Mechanics, 2013. **53**(8): p. 1333-1341.

11. Carroll, J., et al., *An experimental methodology to relate local strain to microstructural texture.* Review of Scientific Instruments, 2010. **81**(8): p. 083703.

12. Kammers, A.D. and S. Daly, *Digital image correlation under scanning electron microscopy: methodology and validation.* Experimental Mechanics, 2013. **53**(9): p. 1743-1761.

13.   Padilla, H., et al., *Relating inhomogeneous deformation to local texture in zirconium through grain-scale digital image correlation strain mapping experiments.* International Journal of Solids and Structures, 2012. **49**(1): p. 18-31.

14.   Chemisky, Y., et al., *Analysis of the deformation paths and thermomechanical parameter identification of a shape memory alloy using digital image correlation over heterogeneous tests.* International Journal of Mechanical Sciences, 2015. **96**: p. 13-24.

15.   Berryman, J.G., *Measurement of spatial correlation functions using image processing techniques.* Journal of Applied Physics, 1985. **57**(7): p. 2374-2384.

16.   Blair, S.C., P.A. Berge, and J.G. Berryman, *Using two-point correlation functions to characterize microgeometry and estimate permeabilities of sandstones and porous glass.* Journal of Geophysical Research: Solid Earth, 1996. **101**(B9): p. 20359-20375.

17.   Jianzhuang, L., L. Wenqing, and T. Yupeng. *Automatic thresholding of gray-level pictures using two-dimension Otsu method.* in *Circuits and Systems, 1991. Conference Proceedings, China., 1991 International Conference on.* 1991. IEEE.

18.   Chang, S., et al., *Direct visualization and three-dimensional reconstruction of structures formed by electrophotographic toner.* Powder Technology, 2015. **269**: p. 1-6.

19.   Duda, R.O. and P.E. Hart, *Use of the Hough Transformation to Detect Lines and Curves in Pictures.* Communications of the ACM, 1972. **15**(1): p. 11-15.

20.   Blaber, J., B. Adair, and A. Antoniou, *Ncorr: open-source 2D digital image correlation matlab software.* Experimental Mechanics, 2015. **55**(6): p. 1105-1122.

21.   Blaber, J., B.S. Adair, and A. Antoniou, *A methodology for high resolution digital image correlation in high temperature experiments.* Review of Scientific Instruments, 2015. **86**(3): p. 035111.

22.   Richeton, T., G. Wang, and C. Fressengeas, *Continuity constraints at interfaces and their consequences on the work hardening of metal–matrix composites.* Journal of the Mechanics and Physics of Solids, 2011. **59**(10): p. 2023-2043.

23.   Franciosi, P., M. Berveiller, and A. Zaoui, *Latent hardening in copper and aluminium single crystals.* Acta Metallurgica, 1980. **28**(3): p. 273-283.

24.   Hosford, W.F., R.L. Fleischer, and W.A. Backofen, *Tensile deformation of aluminum single crystals at low temperatures.* Acta Metallurgica, 1960. **8**(3): p. 187-199.

25.   Bertin, N., et al., *On the strength of dislocation interactions and their effect on latent hardening in pure Magnesium.* International Journal of Plasticity, 2014. **62**: p. 72-92.

26.   Wen, W., et al., *A Physics-Based Crystallographic Modeling Framework for Describing the Thermal Creep Behavior of Fe-Cr Alloys.* Metallurgical and Materials Transactions A, 2017. **48**(5): p. 2603-2617.

27.   Agnew, S.R., M.H. Yoo, and C.N. Tomé, *Application of texture simulation to understanding mechanical behavior of Mg and solid solution alloys containing Li or Y.* Acta Materialia, 2001. **49**(20): p. 4277-4289.

28.   Berbenni, S., V. Favier, and M. Berveiller, *Impact of the grain size distribution on the yield stress of heterogeneous materials.* International Journal of Plasticity, 2007. **23**(1): p. 114-142.

29.   Abe, F., *Precipitate design for creep strengthening of 9% Cr tempered martensitic steel for ultra-supercritical power plants.* Science and Technology of Advanced Materials, 2008. **9**(1): p. 013002.

30.   Ashby, M.F., *A first report on deformation-mechanism maps.* Acta Metallurgica, 1972. **20**(7): p. 887-897.

31.   Wang, H., et al., *A crystal plasticity model based on transition state theory.* International Journal of Plasticity, 2017. **93**: p. 251-268.

32.   Franciosi, P. and A. Zaoui, *Multislip in f.c.c. crystals a theoretical approach compared with experimental data.* Acta Metallurgica, 1982. **30**(8): p. 1627-1637.

33.   Lucas, G.E., *The evolution of mechanical property change in irradiated austenitic stainless steels.* Journal of Nuclear Materials, 1993. **206**(2): p. 287-305.

34.   Qin, Y., G. Götz, and W. Blum, *Subgrain structure during annealing and creep of the cast martensitic Cr-steel G-X12CrMoWVNbN 10-1-1.* Materials Science and Engineering: A, 2003. **341**(1): p. 211-215.

35.   Sobie, C., N. Bertin, and L. Capolungo, *Analysis of Obstacle Hardening Models Using Dislocation Dynamics: Application to Irradiation-Induced Defects.* Metallurgical and Materials Transactions A, 2015. **46**(8): p. 3761-3772.

36.   Clifton, R.J., *On the Analysis of Elastic/Visco-Plastic Waves of Finite Uniaxial Strain.* Shock Waves and the Mechanical Properties of Solids, 1971: p. 73-116.

37.   Lloyd, J.T., et al., *Plane wave simulation of elastic-viscoplastic single crystals.* Journal of the Mechanics and Physics of Solids, 2014. **69**: p. 14-32.

38.   Austin, R.A., D.L. McDowell, and D. Benson, *The deformation and mixing of several Ni/Al powders under shock wave loading: effects of initial configuration.*

Modelling and Simulation in Materials Science and Engineering, 2014. **22**(2): p. 025018.

39. Austin, R.A. and D.L. McDowell, *A dislocation-based constitutive model for viscoplastic deformation of fcc metals at very high strain rates.* International Journal of Plasticity, 2011. **27**(1): p. 1-24.

40. Hirth, J.P., J. Lothe, and T. Mura, *Theory of Dislocations (2nd ed.).* Journal of Applied Mechanics, 1983. **50**(2): p. 476-477.

41. Kocks, U., A. Argon, and M. Ashby, *Thermodynamics and Kinetics of Slip.* Progress in Materials Science, 1975. **19**.

42. Granato, A.V., et al., *Entropy Factors for Thermally Activated Unpinning of Dislocations.* Journal of Applied Physics, 1964. **35**(9): p. 2732-2745.

43. Dong, Y., T. Nogaret, and W.A. Curtin, *Scaling of Dislocation Strengthening by Multiple Obstacle Types.* Metallurgical and Materials Transactions A, 2010. **41**(8): p. 1954-1960.

44. Lagerpusch, U., et al., *Double strengthening of copper by dissolved gold-atoms and by incoherent SiO2-particles: how do the two strengthening contributions superimpose?* Acta Materialia, 2000. **48**(14): p. 3647-3656.

45. Patra, A. and D.L. McDowell, *Crystal plasticity-based constitutive modelling of irradiated bcc structures.* Philosophical Magazine, 2012. **92**(7): p. 861-887.

46. Was, G., *Fundamentals of Radiation Materials Science.* 2 ed. Metals and Alloys. 2017, New York: Springer-Verlag New York. 1002.

47. Bakó, B., et al., *Dislocation dynamics simulations with climb: kinetics of dislocation loop coarsening controlled by bulk diffusion.* Philosophical Magazine, 2011. **91**(23): p. 3173-3191.

48. Geers, M.G.D., et al., *Coupled glide-climb diffusion-enhanced crystal plasticity.* Journal of the Mechanics and Physics of Solids, 2014. **70**: p. 136-153.

49. Gu, Y., et al., *Three-dimensional formulation of dislocation climb.* Journal of the Mechanics and Physics of Solids, 2015. **83**: p. 319-337.

50. Mordehai, D., et al., *Introducing dislocation climb by bulk diffusion in discrete dislocation dynamics.* Philosophical Magazine, 2008. **88**(6): p. 899-925.

51. Hartley, C.S., *A method for linking thermally activated dislocation mechanisms of yielding with continuum plasticity theory.* Philosophical Magazine, 2003. **83**(31-34): p. 3783-3808.

52. Lebensohn, R.A., et al., *Modeling the mechanical response of polycrystals deforming by climb and glide.* Philosophical Magazine, 2010. **90**(5): p. 567-583.

53. Lebensohn, R.A., et al., *Improved constitutive description of single crystal viscoplastic deformation by dislocation climb.* Comptes Rendus Mécanique, 2012. **340**(4): p. 289-295.

54. Weertman, J., *The Peach–Koehler equation for the force on a dislocation modified for hydrostatic pressure.* The Philosophical Magazine: A Journal of Theoretical Experimental and Applied Physics, 1965. **11**(114): p. 1217-1223.

55. Weertman, J., Weertman J.R., *Elementary dislocation theory.* Microscopy Research and Technique, 1993. **25**(2): p. 187-187.

56. Mendelev, M.I. and Y. Mishin, *Molecular dynamics study of self-diffusion in bcc Fe.* Physical Review B, 2009. **80**(14): p. 144111.

57. Kitayama, K., et al., *A crystallographic dislocation model for describing hardening of polycrystals during strain path changes. Application to low carbon steels.* International Journal of Plasticity, 2013. **46**: p. 54-69.

58. Wen, W., et al., *Mechanical behavior of Mg subjected to strain path changes: Experiments and modeling.* International Journal of Plasticity, 2015. **73**: p. 171-183.

59. Wen, W., et al., *Mechanical behavior of low carbon steel subjected to strain path changes: Experiments and modeling.* Acta Materialia, 2016. **111**: p. 305-314.

60. Estrin, Y., *Dislocation theory based constitutive modelling: foundations and applications.* Journal of Materials Processing Technology, 1998. **80-81**: p. 33-39.

61. Nes, E., *Modelling of work hardening and stress saturation in FCC metals.* Progress in Materials Science, 1997. **41**(3): p. 129-193.

62. Kocks, U.F. and H. Mecking, *Physics and phenomenology of strain hardening: the FCC case.* Progress in Materials Science, 2003. **48**(3): p. 171-273.

63. Mecking, H. and U.F. Kocks, *Kinetics of flow and strain-hardening.* Acta Metallurgica, 1981. **29**(11): p. 1865-1875.

64. Beyerlein, I.J. and C.N. Tomé, *A dislocation-based constitutive law for pure Zr including temperature effects.* International Journal of Plasticity, 2008. **24**(5): p. 867-895.

65. Roters, F., D. Raabe, and G. Gottstein, *Work hardening in heterogeneous alloys—a microstructural approach based on three internal state variables.* Acta Materialia, 2000. **48**(17): p. 4181-4189.

66. Hecht, F., *New development in freefem++*, in *Journal of Numerical Mathematics*. 2012. p. 251.

67. Karypis, G. and V. Kumar, *A Fast and High Quality Multilevel Scheme for Partitioning Irregular Graphs.* SIAM Journal on Scientific Computing, 1998. **20**(1): p. 359-392.

68. Satish Balay, S.A., Mark~F. Adams,Jed Brown,Peter Brune,Kris Buschelman,Lisandro Dalcin,Victor Eijkhout,William~D. Gropp,Dinesh Kaushik,Matthew~G. Knepley,Dave~A. May,Lois Curfman McInnes,Richard Tran Mills,Todd Munson,Karl Rupp,Patrick Sanan,Barry~F. Smith and Stefano Zampini,Hong Zhang,Hong Zhang. *PETSc Web page.* 2018; Available from: http://www.mcs.anl.gov/petsc.

69. Dundulis, G., et al., *Numerical and experimental investigation of low cycle fatigue behaviour in P91 steel.* Engineering Failure Analysis, 2017. **79**: p. 285-295.

70. F., L.F. and P.Y. A., *Effect of "Forest" Dislocations in the {1122} ⟨1123⟩ system on hardening in Mg single crystals under basal slip.* physica status solidi (a), 1975. **32**(1): p. 227-232.

71. Basirat, M., et al., *A study of the creep behavior of modified 9Cr–1Mo steel using continuum-damage modeling.* International Journal of Plasticity, 2012. **37**: p. 95-107.

72. Needleman, A. and J.R. Rice, *Plastic creep flow effects in the diffusive cavitation of grain boundaries.* Acta Metallurgica, 1980. **28**(10): p. 1315-1332.

73. Gurland, J., *Observations on the fracture of cementite particles in a spheroidized 1.05% c steel deformed at room temperature.* Acta Metallurgica, 1972. **20**(5): p. 735-741.

74. Argon, A.S., J. Im, and R. Safoglu, *Cavity formation from inclusions in ductile fracture.* Metallurgical Transactions A, 1975. **6**(4): p. 825.

75. Chu, C.C. and A. Needleman, *Void Nucleation Effects in Biaxially Stretched Sheets.* Journal of Engineering Materials and Technology, 1980. **102**(3): p. 249-256.

76. Needleman, A. and V. Tvergaard, *An analysis of ductile rupture modes at a crack tip.* Journal of the Mechanics and Physics of Solids, 1987. **35**(2): p. 151-183.

77. McClintock, F.A., *A criterion for ductile fracture by the growth of holes.* Journal of applied mechanics, 1968. **35**(2): p. 363-371.

78. McClintock, F.A., S.M. Kaplan, and C.A. Berg, *Ductile fracture by hole growth in shear bands.* International Journal of Fracture Mechanics, 1966. **2**(4): p. 614-627.

79. Rice, J.R., Tracey, Dennis Michael, *On the ductile enlargement of voids in triaxial stress fields**. Journal of the Mechanics and Physics of Solids, 1969. **17**(3): p. 201-217.

80. Budiansky, B., J. Hutchinson, and S. Slutsky, *Void growth and collapse in viscous solids*, in *Mechanics of Solids: The Rodney Hill 60th Anniversary Volume*. 1982, Elsevier. p. 13-45.

81. Hull, D. and D.E. Rimmer, *The growth of grain-boundary voids under stress.* The Philosophical Magazine: A Journal of Theoretical Experimental and Applied Physics, 1959. **4**(42): p. 673-687.

82. Chuang, T.-J., et al., *Overview no. 2: Non-equilibrium models for diffusive cavitation of grain interfaces.* Acta Metallurgica, 1979. **27**(3): p. 265-284.

83. Chen, I.W. and A.S. Argon, *Diffusive growth of grain-boundary cavities.* Acta Metallurgica, 1981. **29**(10): p. 1759-1768.

84. Tvergaard, V. and A. Needleman, *Analysis of the cup-cone fracture in a round tensile bar.* Acta Metallurgica, 1984. **32**(1): p. 157-169.

85. Goods, S.H. and L.M. Brown, *Overview No. 1: The nucleation of cavities by plastic deformation.* Acta Metallurgica, 1979. **27**(1): p. 1-15.

86. Andersson, H., *Analysis of a model for void growth and coalescence ahead of a moving crack tip.* Journal of the Mechanics and Physics of Solids, 1977. **25**(3): p. 217-233.

87. Gurson, A.L., *Plastic Flow and Fracture Behavior of Ductile Materials Incorporating Void Bucleation, Growth, and Interaction*, in *Applied Mechanics*. 1975, Brown University: Providence, RI.

88. Gaffard, V., *Experimental study and modelling of high temperature creep flow and damage behaviour of 9Cr1Mo-NbV steel weldments*, in *Materials Science*. 2004, Ecole des Mines de Paris: Paris, FR.